IZMIR KATIP CELEBI UNIVERSITY

GRADUATE SCHOOL OF NATURAL AND APPLIED SCIENCES

DEVELOPMENT OF 3D-PRINTED PLASTIC BASED LOW-COST SENSING SYSTEMS

Ph.D. THESIS

Abdullah BAYRAM

Department of Materials Science and Engineering

JUNE 2018

IZMIR KATIP CELEBI UNIVERSITY

GRADUATE SCHOOL OF NATURAL AND APPLIED SCIENCES

DEVELOPMENT OF 3D-PRINTED PLASTIC BASED LOW-COST SENSING SYSTEMS

PhD. THESIS

Abdullah BAYRAM
(D130111013)

Department of Materials Science and Engineering

Thesis Advisor: Prof. Dr. Serafettin DEMIC

JUNE 2018

İZMİR KÂTİP ÇELEBİ ÜNİVERSİTESİ
FEN BİLİMLERİ ENSTİTÜSÜ

3B-BASKILI PLASTİK BAZLI DÜŞÜK MALİYETLİ ALGILAMA SİSTEMLERİNİN GELİŞTİRİLMESİ

DOKTORA TEZİ

Abdullah BAYRAM
(D130111013)

Malzeme Bilimi ve Mühendisliği Anabilim Dalı

Tez Danışmanı: Prof. Dr. Şerafettin DEMİÇ

HAZIRAN 2018

v

Abdullah BAYRAM, a PhD. student of IKCU **Graduate School of Natural and Applied Sciences**, successfully defended the thesis entitled **"DEVELOPMENT OF 3D-PRINTED PLASTIC BASED LOW-COST SENSING SYSTEMS"**, which he prepared after fulfilling the requirements specified in the associated legislations, before the jury whose signatures are below.

Thesis Advisor: **Prof. Dr. Şerafettin Demiç**   ....
Izmir Katip Çelebi University

Jury Members: **Assoc. Prof. Dr. Mehmet E. Solmaz**   ....
Izmir Katip Celebi University

Prof. Dr. Metin Hüseyin Sabuncu   ....
Dokuz Eylul University

Prof. Dr. Kadriye Ertekin   ....
Dokuz Eylul University

Assoc. Prof. Dr. Fethullah Güneş   ....
Izmir Katip Celebi University

Date of Submission: 30 May 2018
Date of Defense: 25 June 2018

To my family,

FOREWORD

TABLE OF CONTENTS

ABBREVIATIONS

3D	: Three Dimensional
BPA	: Bisphenol-A
2D	: Two Dimensional
PDMS	:Polydimethylsiloxane
PMMA	: Poly(methly methacrylate)
CAD	: Computer-aided Desing
FSC	: Forward Scattered
SSC	: Side Scattered
FSL	: Forward Scattered Light
SSL	: Side Scattered Light
PBS	: Phosphate Buffer Solution
ABS	: Acrylonitrile Butediene Styrene
NTU	: Nepholometric Turbidity Unit

LIST OF TABLES

LIST OF FIGURES

DEVELOPMENT OF 3D-PRINTED PLASTIC BASED LOW-COST SENSING SYSTEMS

ABSTRACT

Environment and health is two important things that are so important to human life because they cannot be separated from each other. The problems related with these two events will negatively affect human life. Therefore, health and environmental problems should be monitored with proper testing devices and analyzed. In order to perform these tests, we need cheap, reliable and fast test equipment. With the revolution of three-dimensional (3D) printing technology that is cheap, practical, fast method of production, this kind of test devices can be produced. This production method is used to produce the device for microfluidics and also it converts smartphones to laboratory infrastructure.

In the current study, on-site test equipment was produced via 3D printing methods and tested for three different applications. In the first study a low cost, reusable flow cytometry device was produced and tested. Thin and thick glass pipes were integrated in the 3D printed aligner. A 3D focus-awareness test and 6-micron particle count tests were performed. The results show that the flow cytometer produced by three-dimensional printer can replace conventional flow cytometers. The second study, a 3D printer was used to produce a special cradle and an immersion apparatus for a smartphone, and identify the most commonly known chemical Bisphenol-A which is harmful to the endocrine system. Quantities of Bisphenol-A in pure water and commercial water were analyzed through a system combining two fiber cables and the phone's flashlight and camera. The resulting photographs were transferred to a computer for color analysis and the results were extracted through image process method. In the third study a portable turbidity measurement device was fabricated for environmental application, consisting of plastic parts, fiber cables and specially designed cradle. Here, formazine standard solutions were used for turbidity measurement. Turbidity meter device can perform measurements both using the scattering and transmission characteristics of light simultaneously.

Keywords: Microfluidic device, Three Dimensional Printers, Spectrometer, Turbidimeter, Color Analysis

3B-BASKILI PLASTİK BAZLI DÜŞÜK MALİYETLİ ALGILAMA SİSTEMLERİNİN GELİŞTİRİLMESİ

ÖZET

Çevre ve sağlık, insan yaşamı için çok önemli ve birbirlerinden ayrılamayacak olan iki önemli şeydir. Bu iki olayla ilgili problemler insan yaşamını olumsuz yönde etkileyecektir. Bu nedenle sağlık ve çevre sorunları uygun test cihazları ile izlenmeli ve analiz edilmelidir. Bu testleri gerçekleştirmek için ucuz, güvenilir ve hızlı test ekipmanına ihtiyaç vardır. Ucuz, pratik, hızlı üretim yöntemi olan üç boyutlu (3B) baskı teknolojisinin devrimiyle bu tür test cihazları üretilebilir. Bu üretim yöntemi mikro akışkanlar için kullanılır ve ayrıca akıllı telefonları laboratuvar altyapısına dönüştürür.

Mevcut çalışmada, yerinde test yöntemi ekipmanları 3B yazıcı yöntemleri kullanılarak üretilmiş ve üç farklı uygulama için test edilmiştir. Birinci çalışmada, düşük maliyetli, tekrar kullanılabilir bir akış sitometresi cihazı üretildi ve test edildi. İnce ve kalın cam borular 3B baskı yöntemi ile üretilmiş plastik hizalayıcıya entegre edildi. Bir 3B odak-farkındalık testi ile 6 mikronluk parçacık sayım testleri gerçekleştirildi. Sonuçlar, üç boyutlu bir yazıcıda üretilen akış sitometrenin geleneksel akış sitometre cihazlarının yerini alabileceğini göstermiştir. İkinci çalışmada, akıllı telefon için özel bir beşik ve bir daldırma aparatı üretmek için 3B yazıcı kullanıldı ve endokrin sistem için en yaygın zararlı kimyasal olarak bilinen bisfenol-a tespiti yapıldı. Saf suda, ticari suda ve musluk suyunda bulunan bisfenol-a miktarları, iki fiber kablo, telefon feneri ve kamerasını birleştiren bir sistem aracılığıyla analiz edildi. Elde edilen fotoğraflar, renk analizi için bir bilgisayara aktarılmış ve sonuçlar görüntü işleme yöntemi ile çıkartılmıştır. Üçüncü çalışmada, çevresel uygulamalar için plastik parçalar, fiber kablolar ve özel olarak tasarlanmış beşikten oluşan taşınabilir bir bulanıklık ölçüm cihazı üretilmiştir. Burada, bulanıklık ölçümü için formazin standart çözeltiler kullanılmıştır. Bulanıklık ölçer cihazından elde edilen sonuçlar hem ışığın saçılımını hem de iletim özelliklerini aynı anda kullanarak ölçümler yapabileceğini göstermiştir.

Anahtar Kelimeler: Mikro akışkan cihaz, Üç boyutlu yazıcılar, turbidimetre, spektrometre, akis sitometresi, renk analizi

1. INTRODUCTION

Health is defined as "A state of complete physical, mental and social well-being and not merely the absence of disease or infirmity" by World Health Organization (WHO) [1]. At first glance, environment and health might be seen separated and irrelevant, actually that is an illusion, because they are close to each other as of result and reason. The best situation explaining relation between health and environment is chicken-egg paradox. Specifically, the basic question is that which come first: the health or the environment. Beyond this discussion, humanity is extremely in need of both, regardless of the priority of one against the other. Namely, future life of the humanity is dependent on welfare of the entire species exist on the environment. Therefore, the more conserved environment, the healthier the humanity. Relatedly, there is a clear but complex interdependence between health and the environment. That is why people are expected to pay inseparable attention to both in order to maintain their lives safely at present and in the future.

At first, we should be aware of the importance of protection of our self-environment and health. Because the environmental pollution is the most known reason for most of the diseases [2-7]. Relatedly, it is a must to measure some reliable quantifies in order to get informed towards the degrees of diseases and environmental pollution. That's why monitoring should be done. The monitoring is defined as detecting changes in the environment and health so as to analysis of routine measurements performance [8]. The monitoring system is defined extensively as a concise description of what should be the objective and a process to determine what is the procedure or status [9]. Mostly, they can be used to calculate the environment or health parameters also. For environmental and health monitoring systems, mostly derive mentioned parameters through considering chemicals, organisms and cells. So, it has vital importance for surveillance and investigation of problems with health and environment [10].

Numerous analytical methods have been employed for the analysis of pollutants and chemicals, and these methods need conventional instrumentation such as high performance liquid chromatography system with ultraviolet spectrophotometer unit (HPLC-UV), HPLC-mass spectrometry (HPLC-MS), gas chromatography-mass spectrometry (GC-MS), ion chromatography (IC), inductively coupled plasma (ICP) and flow cytometers [11-18]. Although these methods can provide accurate and precise results, they mostly require complex instrumentations located in central laboratories with access to specialist labor. The above analysis systems contain many and different types of disadvantages during detection experiments such as more time, excessive chemicals and high cost per analysis. In order to skip those disadvantages, one of the most up-to-date methods for monitoring is to conduct those analyte detection experiments through microfluidic method.

The microfluidic method is a well-known method used for analysis of chemicals, cells and particles for various aim [19]. Its distinctive feature is that the experiment with a microfluidic method requires a very small amount of fluid for which it is famous for that reason it is the cheapest method [20-22]. Due to this basic advantage, researchers recently find it suitable for places struggling with to reach advanced analytical devices to be used in both health and environmental monitoring [23]. Therefore, microfluidic method is a reliable and attractive method for both environmentalists and healthcare providers [19, 24]. Moreover, environment and health monitoring with microfluidic devices is a facile technique and highly open to development.

There are so many production methods of the microfluidic devices, such as micromachining, hot embossing, injection molding and casting [25]. Most of the microfluidic devices seem hard to fabricate in practice. On the other hand, since environmental and health problems are the widespread problem in the whole world, researchers recently emphasize its importance for humanity, as they are powerful candidates for affordable experimenting devices. Namely, they are suitable for resource-limited countries and regions that do not have opportunity to reach expensive equipments. Otherwise, a global solution could not be mentioned. One more important

thing is that, in order to obtain that global solution, it is also necessary to make the apparatus of the monitoring device fully compatible with lab devices which should be reliable and portable as much as possible where, traditional lab equipments are usually expensive, heavy and needs expertise to work on, unfortunately.

Fortunately, hurdles of the health and environmental monitoring problem in the developed countries and rest of the world would be solved thoroughly by new researches based on microfluidic devices. However, as stated above, it is necessary to use lab devices that require expensive and laborious labor in order to collect data from microfluidic devices and to view the result. The way to get rid of this disadvantage is to make imaging through a popular, inexpensive, easy to use and a handy device. Cellular smart phones are now everywhere in the world and this can give unbelievable opportunities for researchers to be used as a handy and clever instrumentation for this purpose [26]. That is because, the smart phones consist advanced sensors and therefore they can easily be converted into a lab device that may maintain "everyone's use" to get a solution. Relatedly, we can say that if we can relocate successive functions of the expensive lab devices into the functions of the cell phones, we may achieve the cheap and affordable monitoring [27-29].

Mentioning above terms, we can summarize the key points as, 1) it is best to use a microfluidic device for examining analytes of health and environment samples, 2) it is best to use existing smartphone devices for the purpose of health&environmental monitoring. 3) In case both the microfluidic mechanism and smart phone device made compatible, a reliable health&environment monitoring will be successfully achieved. 4) The future proposed system should be a cheap solution as much as possible in order to be used in the developed countries and rest of the world.

Fortunately, the complete set of microfluidic and smartphone-based detection systems can be manufactured ensuring the all above requirements successfully. Indeed, the production can be completed through a cheap and moreover a single type of production method [30]. An easy, quick and affordable equipment manufacture method is proposed by 3 dimensional (3D) printing [31] which extremely eased the manufacturing for

3

prototype developers of many devices, including the microfluidics. Namely, the 3D printing method has been a successful candidate for the last thirty years for application in many fields such as architecture, construction, maritime industry, healthcare, medical, chemical industry, mechanics, food industry, automotive, textile and robotics etc. The same compilation can be made true for health&environment monitoring systems, too. Namely, 3D printing technology opens place within lots of array of disciplines with offering good advantages on manufacturing. So it affects variety of the fields from chemistry to biomedical and from electronics to medicine. Therefore, 3D printing technology, with the great impact on numerous fields, is usually named as 3D printing revolution.

The 3D revolution brings flexibility and diversity in many terms. That is to say, 3D printers have a wide range of application types and can be utilized with many different materials. Hence, they are usually classified in a variety of functionalities. Therefore, determining the appropriate printer type is extremely important. All 3D printers require 3D computer aided designed (CAD) models and specific software that discretely slices (layer) 3D models in Z direction. The sliced model allows building a 3D object layer-by-layer. Although various 3D printing methods already exist, many of them still require further development [32]. As mentioned, 3D printing methods can be classified in many types, and, one of the corresponding classification types depends on manufacturing principles. According to manufacturing principles, 3D printers can be divided into extrusion-based, photocuring, photomelting, inkjet-based and paper cutting types. Here, each of printer type offers some distinctive advantages comparing to the others.

Extrusion-based 3D printing is known as fused deposition modeling (FDM). FDM is an open source low-cost technology. It produces objects by extruding melted material from a nozzle [33]. The nozzle follows the paths in the layer, and passes to the upper layers, until the objects are built in Z direction from bottom to top. An extruded layer under each succeeding layer plays a supporting role for the next piled layers [34-36]. This method is based entirely on physical changes of input materials. So far thermoplastics have been widely used as input materials, but more recently powder and liquid forms of

4

thermoplastics, ceramics and various metals became popular for use with FDM as well [37-41]. Consequently, FDM manufacturing method offers advantages in term of material cost, support removal, machine cost and office environmental friendly. Photocuring-based 3D printing is performed using liquid photo-resin materials. Photoinitiators absorb the light and form free radicals that induce bonding of polymers and of monomers, and form the cured film. Ultraviolet (UV) or laser light is used.

Digital Light Processing (DLP) [42] system consists a laser or a UV lamp as a masked light source. The light exposes the photosensitive resin though special patterns on the mask. After the curing of the bottom layer, the stage moves in Z direction and the succeeding layer starts scanning for curing, until the completion of the entire model [43-45]. Consequently, DLP manufacturing method offers advantages in term of surface finish and high resolution.

Up to now, microfluidic devices have been fabricated entirely or partially with the 3D printers so as to apply variety of fields such as organ printing, microfluidic and industrial design [46-49]. So, microfluidic devices are possibly come across in the fields of biological research, cell based researches, chemical synthesis, etc. and they usually perform detection, separation, counting. Moreover, 3D printing facilitates the microfluidics applications of biological research, thanks to the economy, fast producibility and high availability of used materials [50]. Accordingly, the number of publications related to 3D printed microfluidic devices has increased in the last decade [51]. For example, McDonald et al. pioneered the printing of microchips using a solid-based printer for mold printing [52]. In one of the previous study, optimized biosensor device fabrication has been achieved and it was compatible with an electrochemical device [53] . One of the studies reported that pathogenic bacteria have been detected with a 3D-printed device [54]. Moreover, a microfluidic platform was fabricated using a FDM 3D printer with ABS for detection of Methicillin-resistant Staphylo-coccus aureus (MRSA) [55]. Takenaga et al proposed a light addressable potentiometric sensor (LAPS) for chemical sensing [56]. The other interesting application is 3D printed microfluidic device for high throughput drug transport [57]. Also, reusable 3D-printed microfluidic

devices are offered for the electrochemical detection in which it has various electrodes consisting ability for the detection of neurotransmitter, nitric oxide [58]. Again, Electrochemical detection of hydrolyzed micro RNA has been achieved with FDM 3D printing with ABS material [59]. In 2015, Gao et al. presented cell-laden hydrogel 3D-printed micro channel structures for nutrient distribution [60]. Bargawa et al. proposed a large-scale 3D modular microfluidic system, composed of 3D-printed discrete elements and rapidly reconfigurable parts [61]. Jue et al. reported using a 3D-printed meter-mix device for urine measurement and lysing [62]. Gowers et al. achieved continuous monitoring of glucose and lactate levels in tissue through integration of a 3D-printed microfluidic device and electrodes [31]. Lockwood et al. reported utilizing a 3D-printed device to show in-vitro pharmaco-kinetic profiling of molecules [63]. In this research, the device includes separately porous membrane wells integrated with multiple flow channels. The membranes allow diffusion of small molecules between wells and channels.

The 3D printer revolution not only affected microfluidics, but also enabled the average person to use their smartphone as a functional laboratory device and an analyzer [64-67]. In the process, a smartphone is modified with a 3D-printed apparatus to imitate the basic features of the analyzing instrument. Proximity sensor, temperature sensor, especially camera – usually prebuilt into smartphones by default – are used as data receiving components. These days smartphones are applied to many fields, such as colorimetric biosensors, surface plasmon resonance devices, photoluminescence biosensors, chemical-luminescence-based detection, electrochemical biosensors, bioluminescence-based detection and microscopy [68]. For example, in 2011, POC application of a smartphone as a biosensor was reported by Delaney et al. [69]. Since, smartphones integrated with biosensors have attracted further attention in the context of various instrumental transduction technologies, and the number of applications reported has grown [70-73]. Researchers have focused on smartphone applications because phones' its in-built cameras have simplified the measurement of absorbance or reflectance from solution, and opened a pathway for colorimetric biosensors assays. In one of the pioneering works published by Shen et al., quantified colors were measured on paper

strips for diagnostic assays [71, 74]. Breslaur et al reported a microscope-integrated smartphone to capture bright field and fluorescence imaging [75]. The system has compact apparatus and contains optical elements such as emission filter, light emitting diode, collector lens, condenser lens, microscope eyepiece and objective. Another smartphone-based lens-free microscope was reported by Tseng et al [76]. It incorporates a very simple design that does not compromise any optical components, lenses or lasers. In this design, a vertical illuminated LED light is scattered, refracted and transmitted after interaction with the sample. Among these lights the transmitted light waves produce a hologram of samples detectable by smartphone cameras. The proposed system takes images of parasites, red and white blood cells and micro particles. In addition to the previous applications, various approaches have been proposed to develop smartphone fluorescent microscopes [29, 77], fiber optic component assisted smartphone microscopes [78, 79], and a rapid diagnostic test platform [80].

This thesis introduces the application of plastic-based sensing systems to biomedical and environmental practices. The scope and guidelines of each part are presented below.

In this part, health and environment was defined and their importance and relations were revealed. Possible detrimental materials, the reasons of those damages, and precautions were discussed. Detailed information was given about health and environment monitoring. Additionally, the traditional monitoring types and production methods of the sensing systems were shortly mentioned. 3D printing approaches was detailed and some monitoring device examples, produced by 3D printing, for health and environment were given.

The second part is about theoretical background of the thesis in which light materials interaction phenomenon and diffraction grating physics were given.

The third part presents a facile strategy for fabricating a microfluidic flow cytometer, using two glass micropipettes of different sizes. A 3D-printed millifluidic aligner for alignment of the manufactured micropipettes is described. Particle confinement in micropipettes is achieved by hydrodynamic focusing, using a single sample and sheath flow. Device performance is evaluated using the forward and side-scattered optical

7

signals obtained by fiber-coupled laser and photodetectors. The 3D-printed assisted glass capillary microfluidic device is ultra-low-cost and labor-efficient, and its fabrication takes under 10 minutes. This device offers a great alternative to conventional benchtop flow cytometers in terms of optofluidic configuration.

In the fourth part, a developed 3D printed portable device that works with a smartphone is introduced. We evaluated our product in relation to colorimetric sensing methods, since the product is specially manufactured for places scarce in sophisticated laboratory environment. A precise fabrication of a low-cost and portable apparatus is particularly beneficial for places where resources are limited. We propose a newly designed, handheld, reflection-based smartphone-sensing platform to detect Bisphenol A (BPA), an endocrine disruptor agent abundantly used in the plastic industry. An experimental investigation that relied on color changes was conducted with samples from two different water sources: distilled and commercial drinking water. This colorimetric measurement device was used to determine BPA in distilled water in alkaline environments. The successful combination of colorimetric assay and spectrometer facilitates limit of detection in the low ppm levels, 0.29 ppm for smartphone and 0.23 ppm for commercial spectrometer, with a sensitivity of 0.1/ppm.

In the fifth part, the smartphone was converted into a turbidimeter to maintain sustainable public health. Custom designed components for the smartphone system were manufactured via a 3D printer. The proposed instrumentation requires no active electrical or optical components, relying on the smartphone's native sensors and software. The smartphone turbidimeter provides an accurate and practical method for field measurement of turbidity, through the collection of transmitted and reflected light. In summary, this study presents the results of manufacturing an ultra-low-cost, portable smartphone turbidimeter, based on both forward and side-scattered lights spectroscopic measurement techniques, created to benefit public health.

In the last part, general conclusion was added.

2. THEORETICAL OVERVIEW

2.1 Introduction

In this part, the fundamental principles of the light-material interaction are briefly explained. Reflection, refraction, absorption, diffraction and scattering events are introduced. Rayleigh and Mie Theory are basically explained. The theories are discussed using the treatments and notations given by Kerker [81].

2.2 Reflection and Refraction of Light

Reflection of light is one of the phenomenon in which incident light bounces from the material surface. The basic physical principle of the light reflection from a smooth surface is shown in Fig. 2.1. Here, the angle between the incident light and mirror surface normal is equal to the angle between reflected light and the normal. Reflection process depends on the reflecting surface by which the light is bounced in many directions. This process is named as diffuse reflection. Reflectivity of surface is defined as the ratio of total intensity of reflected light (I_r) to the total intensity of incident light (I_0). R stands for reflectivity and generally given as $R\%$.

$$R = \frac{I_r}{I_0} \qquad (2.1)$$

Refraction is the other phenomenon known as bending of the light as it passes from one medium to the other.
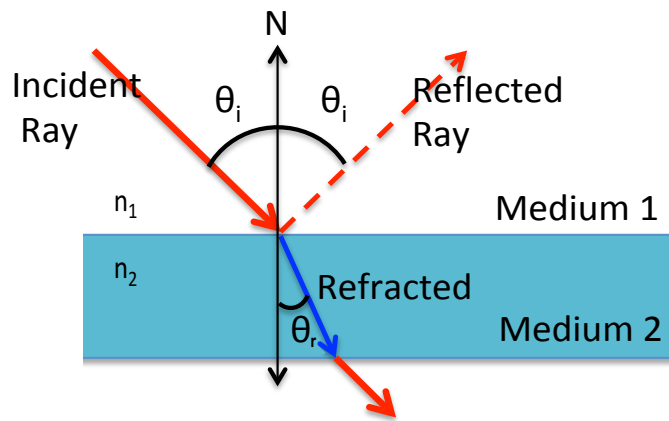
Figure 2.1 : Reflection and refraction of light.

In Fig. 2.1, the refraction of incident light that passes from air medium to water medium is illustrated. The relations between the incident light angle (θ_i), refracted light angle (θ_r), refraction indices (n_1, n_2) have been previously proved by Snell's Law. Here, the refraction indices are defined as the ratio of speed of light in vacuum to speed of light in medium. The Snell's Law is proved via minimum total travelling time from one medium to the other medium.

$$n_1 \sin \theta_i = n_2 \sin \theta_r \tag{2.2}$$

If the refracted light angle (θ_r) is equal to 90°, the light is neither reflected nor refracted. It travels along the interface layer between the two mediums. In this case, θ_i is referred as critical angle.

2.3 Diffraction of Light

In this part, the diffraction of the light from a single slit, double slit, multiple slits and gratings are introduced. The transmission and reflective gratings are emphasized, as well.

Diffraction is a phenomenon that occurs when a wave comes across a barrier or passes through a narrow aperture. When the light passes through the barrier or aperture, it spreads out to the shadow of barrier. As a result, dark and bright fringes occur. These

fringes are called diffraction patterns that consist of central maximum (broad intense central band) and secondary maxima (less intense bands). When taking into account the incident light and screen location, diffraction patterns can be classified in two different types. Namely, when the source or screen is close to the aperture, the incident light wave fronts are spherical. Therefore, the resulted patterns are quite complex. This situation is named as Fresnel diffraction. On the other hand, when both source and screen are distant from each other, the incident light waves are plane waves. Therefore, wave fronts passing through slits are parallel. This is called the Fraunhofer diffraction. The diffraction phenomenon can be examined through single slit diffraction, double slit diffraction and multiple slit diffractions.

The single slit diffraction is the bending of waves when they pass through a long and narrow slit with a length of a.

From Fig. 2.2, the rays r_1 and r_2 at point P_1 cancel each other. In here, a totally destructive interference patterns exist. In single slit diffraction, dark fringes are produced by the path length difference between r_1 and r_2 and are equal to $\lambda, 2\lambda \dots m\lambda$, as follows,

$$a \sin(\theta) = m\lambda \quad for \ m = 1, 2, 3, \dots. \ (minima - dark \ fringes) \qquad (2.3)$$

The intensity of the diffraction pattern located at the angle of θ is given as follows,

$$I(\theta) = I_m \left(\frac{sin\alpha}{\alpha}\right)^2 \ where \ \alpha = \frac{\pi a}{\lambda} \sin\theta \qquad (2.4)$$

where I_m is the intensity at the center of the pattern.
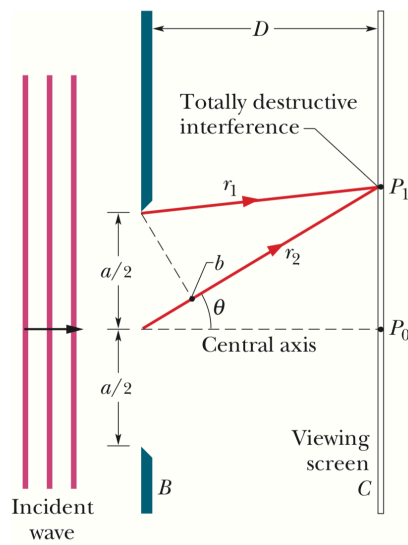
Figure 2.2 : Diffraction from single slit [82].

The diffraction phenomenon in multiple slits can be understood as in the diffraction in double slit or multiple slits. Namely, if the plane light passes through a barrier, the diffraction patterns given in Fig. 2.3 are formed on the screen, located at a distance of x from slit.
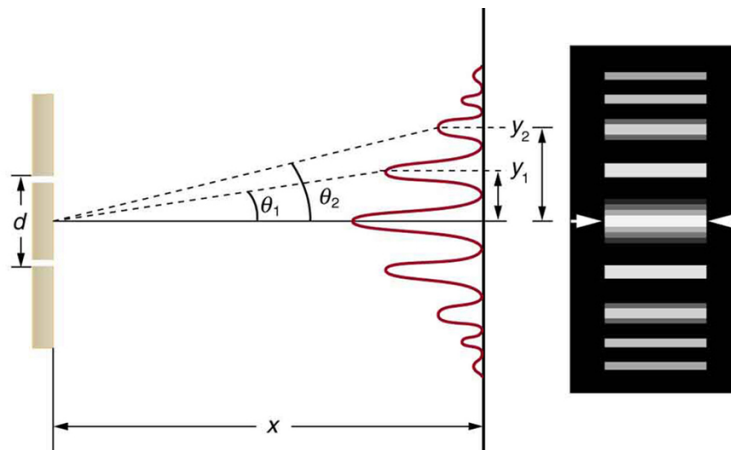
Figure 2.3 : Diffraction of light from double slit [82].

In Fig. 2.3, d is the distance between the two slits, θ_1 is the angle between first order diffracted light pattern and grating normal, θ_2 is the angle for the second order diffracted light pattern. Here, y_1 and y_2 are the distances from the zero-order diffracted light

location to the first and second-order diffracted light location, respectively, where the corresponding relation is expressed as follows,

$$m\lambda = d\sin(\theta) \quad m = \cdots -1, 0, +1 \ldots (maxima) \tag{2.5}$$

where m is diffraction order. Assuming that, each of the slit width is a and the distance between the centers is d, the intensity of the diffraction patterns at the angle of θ is as follows,

$$I(\theta) = I_m(\cos^2 \beta)\left(\frac{sin\alpha}{\alpha}\right)^2 \tag{2.6}$$

where

$$\alpha = \frac{\pi a}{\lambda}\sin\theta, \qquad \beta = \left(\frac{\pi d}{\lambda}\right)\sin(\theta) \tag{2.7}$$

Diffraction grating is an optical component that consists of periodic structures on its surface (Fig.2.4). Here, it diffracts and splits light into several beams travelling in different direction. Amount of the diffraction is depended on the wavelength of incident light and grating space (d) between periodic surface structures. A transmission grating with N slits results in maxima at an angle of θ as follows,

$$d\sin\theta = m\lambda, \qquad for\ m = 0, 1, 2.. (maxima) \tag{2.8}$$
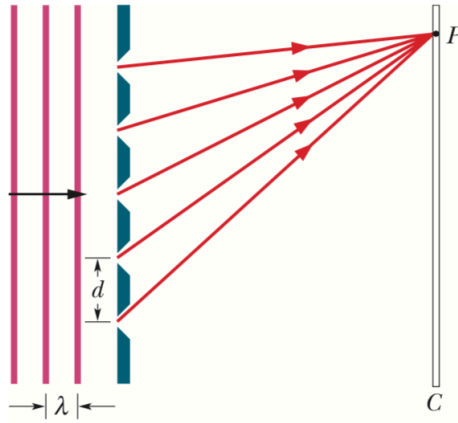
Figure 2.4 : Transmission diffraction grating produces patterns on the screen [82].

Half widths of the lines are stated as follow,

$$\Delta\theta_{hw} = \frac{\lambda}{Nd\cos\theta} \tag{2.9}$$

The grating spreads apart the diffraction lines into various wavelengths. The wavelength distinguishing ability of the grating is defined as dispersion. The dispersion is defined as follows,

$$D = \frac{\Delta\theta}{\Delta\lambda} = \frac{m}{d\cos\theta} \tag{2.10}$$

The limit of resolution of the resulting spectra is defined as resolving power. It is a dimensionless quantity given by the wavelength divided by the limit of resolution. The resolution is the measure of the wavelength difference between the equal intensity neighbors that can be distinguished.

$$R = \frac{\lambda_{avg}}{\Delta\lambda} = Nm \tag{2.11}$$

2.4 Absorption of Light

Both absorption and scattering may occur in any medium where they are named as light extinction when they occur together. Here we can define scattering coefficient (k_s) and absorption coefficient (k_a) are proportional to the number of absorber concentration (c) and cross section area (σ). The overall extinction of light with the wavelength of λ passing through a medium of thickness L is expressed as follows,

$$I(\lambda) = I_0(\lambda)\, e^{(-k_e L)} \tag{2.12}$$

where $k_e = k_a + k_s$, and $I_0(\lambda)$ is the intensity of light entering the medium. This intensity can be expressed using the Beer-Lambert law. Absorbance in molecular range depends on the excitation of electrons from ground states to excited states. Here electrons gain photon energy after striking with photon. In this manner, the more molecules the solution has, the more absorption of light take place. If it is assumed that a sample as in Fig 2.5 is undertaken to the absorbance measurement, absorbance (A) is depended on extinction coefficient, concentration and length of the medium that light travelling and expressed as:

$$A = k_e c L \tag{2.13}$$
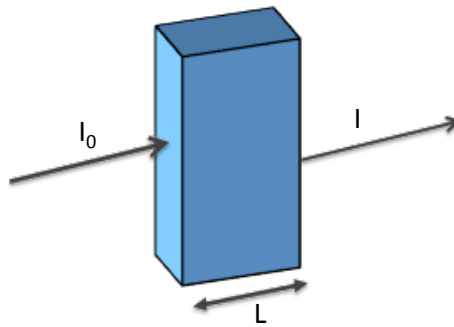
Figure 2.5 : Absorption of light in solution.

2.5 Scattering of Light

The scattering is redirection of the light that occurs when an electromagnetic (EM) wave comes across an obstruction or non-homogenous medium. When the EM waves come across with particles, the constituent molecules of the particles are also affected. Electron orbits are oscillated or perturbed periodically with the same frequency of the incident wave and result in periodic separation of the charge within molecules in which the separation can be visualized as in Fig 2.6.
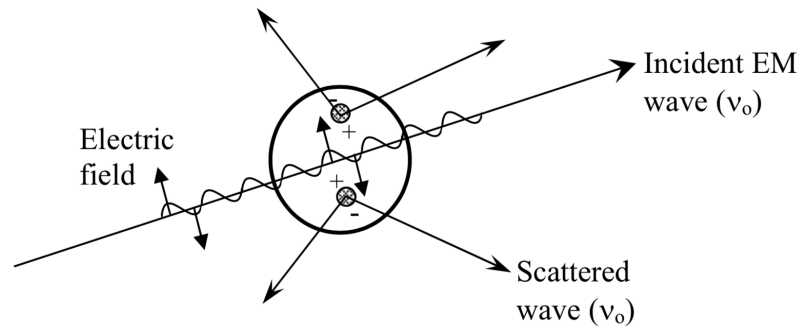
Figure 2.6 : Induced dipole moment and light scattering by an EM wave [83].

This situation is named as induced dipole moment and it behaves as an EM radiation source thereby scattered light exists. The scattered light, emitted by particle, has the same frequency with the incident light and this event called as elastic scattering. Scattering theories can be classified in to two categories. The first one is Rayleigh scattering theory, which is applicable to small, dielectric and spherical particles. The second theory is Mie Scattering theory, which offers comprehensive solutions for generally spherical particles without caring absorbing or non-absorbing particles and size limitations. Accordingly, Mie theory converges to the geometric optic limits for large particles. Therefore, Mie scattering theory is appropriate to describe most of spherical particles including Rayleigh scattering. Particle size limitation for Rayleigh scattering is $\alpha \ll 1$ and $|m|\alpha \ll 1$.

$$\alpha = \frac{2\pi a}{\lambda} \tag{2.14}$$

where α is the dimensionless parameter and expressed as in Equation 2.15 and a is the particle radius. Here, λ is the relative scattering wavelength defined as

$$\lambda = \frac{\lambda_0}{m_0} \tag{2.15}$$

where λ_0 is the wavelength in vacuum and m_0 is the refractive index of the medium.

$$m = n - ik \tag{2.16}$$

where m is the refractive index of the scattered particle. In this notation, n represents refraction of light (resulted from the ratio of the speed in vacuum and material ambient) and complex term is related with absorption. Here, k stands for extinction coefficient. It represents decaying or damping of oscillation amplitude. Absorption coefficient of material (with inverse of cm dimension) is also related this complex part, namely, as follows,

$$absorption\ coefficient = \frac{4\pi k}{\lambda} \tag{2.17}$$

The value of k is never equal to zero but approaches to zero for dielectric materials. The magnitude of the complex part is obtained as follows,

$$|m| = (n^2 + k^2)^{1/2} \tag{2.18}$$

If the particles are sufficiently small, they can encounter uniform electric field. Accordingly, the electric field penetration time is much less than EM wave oscillation period. With using spherical coordinate geometry in Figure 2.7, showing a single spherical particle and a single incident light, Mie and Rayleigh scattering parameters are defined.
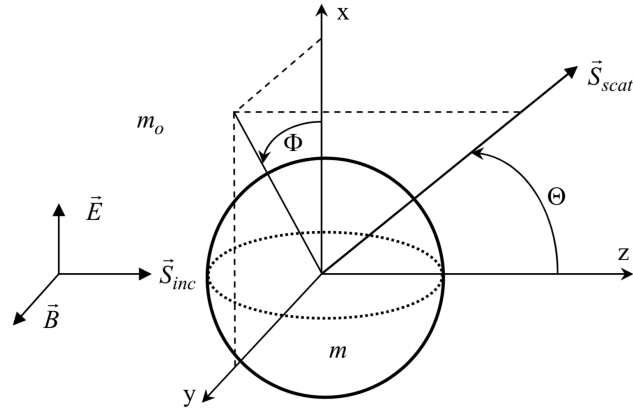
Figure 2.7 : Coordinate geometry [83].

Light is an EM field and can be defined as a time depended function of EM field at the origin in Figure 2.7.

$$E_x = E_0 \cos(\frac{2\pi ct}{\lambda}) \tag{2.19}$$

Here, it is assumed that, this EM field has the amplitude of electric field E_0 and its plane-polarized light along x direction E_x where its wavelength is λ and c denotes speed of light. If interacted particle is a polarizable particle, a dipole moment will be induced due to the incident field. Dipole moment magnitude is proportional to the incident field.

$$p = \alpha_p E_0 \cos(\frac{2\pi ct}{\lambda}) \tag{2.20}$$

where the dipole moment radiates in all directions. As represented in Fig.2.7, the radiated light at the distance r with the angle of θ_x from the x-axis will be assumed for observation. At that point, light field (E_s) will be proportional to ($1/r$) ($1/c^2$) (d^2p/dt^2). Here, the term of ($1/r$) is spatial effect and second derivative of dipole moment is acceleration of charge, respectively. Finally, scattered light field turns into:

$$E_s = \frac{1}{r} x \frac{1}{c^2} x \frac{d^2p}{dt^2} = -\frac{1}{c^2} \alpha_p E_0 \frac{4\pi^2 c^2}{r\lambda^2} sin\theta_x \cos(\frac{2\pi ct}{\lambda}) \tag{2.21}$$

18

Here, detection of electric filed at the distance of r from scattered particle basically is based on intensity of electric field. Light intensity is squared EM field amplitude. Light intensity at a distance of r and at an angle of θ_x is as follows,

$$I_s = \alpha_p^2 I_{0x} \frac{16\pi^4}{r^2 \lambda^4} \sin^2 \theta_x \qquad (2.22)$$

where I_{0x} is the intensity of the incident light polarized in x direction.

$$I_{0x} = E_0^2 \qquad (2.23)$$

Up to now, all derived results are for polarized light where induced dipole moment and intensity of the x-direction polarized light are derived. For the unpolarized light, the results can be derived assuming incident light polarized in both the x direction and y direction as shown in Fig. 2.7.

The scattering radiation intensities on both x-direction and y-direction are thought as vertically and horizontally polarized radiation with respect to the scattering plane. Relatedly, the intensities are defined as follows in terms of angular intensity functions i_1 and i_2.

$$I_\phi = I_0 \frac{\lambda^2}{4\pi^2 r^2} i_1 \sin^2 \phi \qquad (2.24)$$

$$I_\theta = I_0 \frac{\lambda^2}{4\pi^2 r^2} i_2 \cos^2 \phi \qquad (2.25)$$

Polarized incident radiation results in polarized scattered radiation after interacting with particles. The scattering intensities may be written in terms of the polarization states with respect to the scattering plane. Therefore, the intensities can be rewritten in terms of differential scattering cross section as follows,

19

$$I_{VV} = I_0 \frac{1}{r^2} \sigma'_{VV} \tag{2.26}$$

$$I_{HH} = I_0 \frac{1}{r^2} \sigma'_{HH} \tag{2.27}$$

The equations (Equation 2.27, 2.28) are defined with respect to the scattering plane where subscripts refer to vertically polarized and horizontal polarized radiation for both incident radiation and scattered radiation. Overall, subscripts stand for polarization state of the associated radiations. For the unpolarized light, the scattering is found as follows,

$$I_{scat} = I_0 \frac{1}{r^2} \sigma'_{scat} \tag{2.28}$$

where σ'_{scat} is the average of the vertical and horizontal states and just depend on θ resulted from differential cross sections. This intensity of the single scattered light (Equation 2.29) can be rewritten in terms of scattered energy rate with a defined solid angle as illustrated in Fig. 2.8. Here, dA is the scattering cross section area located at the distance of r and $d\omega$ is the solid angle. The total scattering energy rate is considered as follows,

$$E_{scat} = I_0 \sigma'_{scat} d\omega \tag{2.29}$$
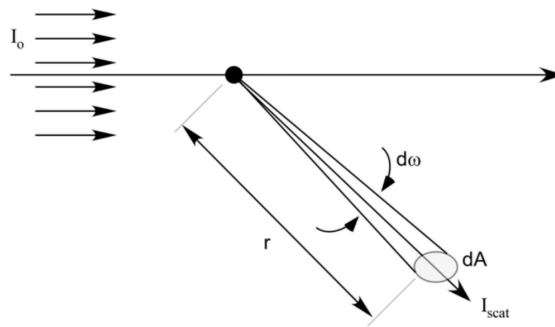
Figure 2.8 : Angular scattering intensity [83].

All above equations consider the distribution of the incident radiation due to the scattering. We note that all the rate of lost energy can be calculated from extinction cross-section expressed in cm^2.

$$E_{removed} = I_0 \sigma_{ext} \tag{2.30}$$

Total energy decrement from the incident beam due to the interaction is expressed as extinction cross-section including absorption and scattering cross section.

$$\sigma_{ext} = \sigma_{abs} + \sigma_{scat} \tag{2.31}$$

The extinction quantity is calculated by integrating the differential cross section over 4π steradians. To express the effect of the particle size or cross-section, Rayleigh and Mie theory will be discussed.

2.5.1 Rayleigh theory

Differential scattering cross sections are expressed as follows,

$$\sigma'_{VV} = \frac{\lambda^2}{4\pi^2} \alpha^6 \left| \frac{\overline{m}^2 - 1}{\overline{m}^2 + 2} \right|^2 \tag{2.32}$$

$$\sigma'_{HH} = \sigma'_{VV} \cos^2 \theta \tag{2.33}$$

Vertical cross sections are proportional to sixth power of the particle size (α) and inverse proportional to the fourth power of the wavelength. Reasonably, the shorter wavelength is redirected and scattered more than the longer wavelength. As an example, the size of air molecules in the atmosphere is within the range of Rayleigh regime and this is the reason why sky appears as blue. Moreover, vertical differential cross section is independent from the angle θ, but horizontal differential cross section is depended on cosine square of θ. By means of that, at the 90° degrees, horizontal differential cross

section is minimum. The total scattering cross section (cm^2) and absorption cross section (cm^2) are defined as follows,

$$\sigma_{scat} = \frac{2\lambda^2}{2\pi} a^6 \left| \frac{\overline{m}^2 - 1}{\overline{m}^2 + 2} \right|^2 \tag{2.34}$$

$$\sigma_{abs} = \frac{-\lambda^2}{\pi} a^3 Im \left| \frac{\overline{m}^2 - 1}{\overline{m}^2 + 2} \right|^2 \tag{2.35}$$

Finally, the total extinction cross section (cm^2) is defined as follows,

$$\sigma_{ext} = \sigma_{abs} + \sigma_{scat} \tag{2.36}$$

Scattering cross section is depended sixth power of the particles size while the absorbance cross section is depended on the third power. Due to the particle size dependency, total extinction reasons can be resulted either from the absorbance or scattering. All in all, if the particles are absorbing-particles (k≠0), total extinction cross section is equal to the total absorbing cross section. If k=0, total extinction cross section is equal to the total scattering cross section.

2.5.2 Mie theory

Mie theory is a powerful theory and offers an exact solution. It offers advantages in terms of particle size, refractive index and efficient scatter. Mie theory is limited to spherical particles. Basically, Mie theory is a rigorous solution of the Maxwell's equations applied to the scattering of plane waves of a spherical particle. Concept of the problem is based on EM wave interacted with spherical particle located in a vacuum.

Maxwell's equations are used to explain the phenomenon occurs on the boundary of the particle and vacuum. The differential scattering cross sections are as follows,

$$\sigma'_{VV} = \frac{\lambda^2}{4\pi^2} i_1 \qquad (2.37)$$

$$\sigma'_{HH} = \frac{\lambda^2}{4\pi^2} i_2 \qquad (2.38)$$

where i_1 and i_2 are angular intensity functions. Remember that, the differential scattering cross section for unpolarized incident light is expressed as follows,

$$\sigma'_{scat} = \frac{\lambda^2}{8\pi^2} (i_1 + i_2) \qquad (2.39)$$

where i_1 and i_2 are calculated from the following infinite series

$$i_1 = \left| \sum_{n=1}^{\infty} \frac{2n+1}{n(n+1)} [a_n \pi_n(\cos\theta) + b_n \tau_n(\cos\theta)] \right|^2 \qquad (2.40)$$

$$i_2 = \left| \sum_{n=1}^{\infty} \frac{2n+1}{n(n+1)} [a_n \tau_n(\cos\theta) + b_n \pi_n(\cos\theta)] \right|^2 \qquad (2.41)$$

where the angular intensity functions π_n and τ_n are defined in terms of the Legendre polynomials

$$\pi_n(\cos\theta) = \frac{P_n^{(1)}(\cos\theta)}{\sin\theta} \qquad (2.42)$$

$$\tau_n(\cos\theta) = \frac{dP_n^{(1)}(\cos\theta)}{d\theta} \tag{2.43}$$

where a_n and b_n are defined as follows,

$$a_n = \frac{\Psi_n(\alpha)\Psi_n'(m\alpha) - m\Psi_n(m\alpha)\Psi_n'(\alpha)}{\xi(\alpha)\Psi_n'(m\alpha) - m\Psi_n(m\alpha)\xi_n'(\alpha)} \tag{2.44}$$

$$b_n = \frac{m\Psi_n(\alpha)\Psi_n'(m\alpha) - \Psi_n(m\alpha)\Psi_n'(\alpha)}{m\xi(\alpha)\Psi_n'(m\alpha) - \Psi_n(m\alpha)\xi_n'(\alpha)} \tag{2.45}$$

where size parameter (α) is as follows,

$$\alpha = \frac{2\pi a m_0}{\lambda_0} \tag{2.46}$$

Regarding the a_n and b_n parameters, Ψ and ξ are Ricatti-Bessel functions. They are expressed in terms of Bessel function.

$$\Psi_n(z) = \left(\frac{\pi z}{2}\right)^{\frac{1}{2}} J_{n+\frac{1}{2}}(z) \tag{2.47}$$

the parameter ξ_n is defined as follows,

$$\xi_n(z) = \left(\frac{\pi z}{2}\right)^{\frac{1}{2}} H_{n+\frac{1}{2}}(z) = \Psi_n(z) + iX_n(z) \tag{2.48}$$

Here, $H_{n+1/2}(z)$ is defined as half integer order Henkel function (second kind). X_n is expressed in terms of half-integer-order Bessel function (second kind). Namely, it is given as follows,

$$X_n(z) = -\left(\frac{\pi z}{2}\right)^{\frac{1}{2}} Y_{n+\frac{1}{2}}(z) \tag{2.49}$$

24

Finally, the extinction cross section and scattering cross section are derived as in the following equations.

$$\sigma_{ext} = \frac{\lambda^2}{2\pi} \sum_{n=0}^{\infty} (2n + 1)Re(a_n + b_n) \qquad (2.50)$$

$$\sigma_{scat} = \frac{\lambda^2}{2\pi} \sum_{n=0}^{\infty} (2n + 1)(|a_n|^2 + |b_n|^2) \qquad (2.51)$$

3. INTEGRATION OF GLASS MICROPIPETTES WITH 3D PRINTER ALIGNER FOR MICROFLUIDIC FLOW CYTOMETRY

3.1 Introduction

Flow cytometry has become one of the most powerful techniques in research and clinical laboratories for a variety of applications ranging from analyzing the physical and chemical properties of particles to high-throughput single cell analysis, and even measuring cancer biomarkers. Flow cytometry has proven to be a sensitive, quantitative and as well as non-invasive approach to obtaining valuable information from single cells [17, 84-86]. It is routinely used in clinical laboratories for the identification and classification of certain cancers, such as leukemia[87-89] and lymphoma[90, 91], and even for the diagnosis of life-threatening diseases such as AIDS [92, 93]. Because of the disadvantages of the conventional benchtop flow cytometers such as high cost, large size, maintenance, complex configuration and the necessity to consume large volumes of expensive reagents, a great deal of attention has been paid to fabricate microfluidic devices using microfabrication technology in recent years. Microfluidic devices have the potential to replace the conventional benchtop flow cytometers and also lead the change to personalized healthcare medicine through point-of-care diagnostics as they offer many advantages like simplicity, low cost, low consumption of reagents, rapid analysis, small size and high controllability in fluid-particle-cell manipulation. All flow based systems have one thing in common which is to confine the sample being analyzed close to the center of the channel so that samples can pass though the interrogation area one at a time, a phenomenon that improves the precision and accuracy of the detection and also lowers the possibility of channel clogging and sample adsorption to the channel wall. A variety of focusing methods exploiting different physical mechanisms have been developed; hydrodynamic focusing [94-97], dielectrophoresis [98, 99], acoustics [100-103] and electroosmosis [104-106]. Hydrodynamic focusing enables focusing in a wide velocity range and has no special requirement for particles, cells and fluids used as expected in a conventional flow-cytometer. Basically, it is usually used to guide

particles or cells in a confined space by manipulating the streamlines. Despite the large number of studies devoted to 2D hydrodynamic focusing whose sample flow is focused only horizontally, the lack of vertical focusing called for the development of 3D hydrodynamic focusing devices that are capable of focusing the stream of particles or cells both vertically and horizontally. Confining the stream of particles in multiple directions ensures the uniform flow of particles through the detection area, which improves a number of features of the microfluidic flow cytometers including performance, accuracy, stability, sensitivity and as well as detection resolution [97, 107, 108]. Up to date, different 3D focusing strategies have been proposed to fabricate microfluidic devices; for example, Sundararajan et al. used six sheath inlets and a five-layer design for 3D focusing of sample fluid in flow [109]. The use of multiple syringes and multiple layer fabrication made the design rather complicated. Gorthi et al. fabricated a PDMS based single-layer microfluidic device that consists of three inlets (one for sample flow and two for sheath flow) and an outlet to realize hydrodynamic 3D flow focusing [94]. Even though PDMS device fabrication involved a single layer, the master required for replica molding and the device fabrication required multilayer fabrication by means of photolithography. Testa et al. developed a micro-flow cytometer capable of self-aligned 3D hydrodynamic focusing [95]. To make the device, the design was first printed on two 3 mm-thick PMMAs using a high precision computer numerical control micromilling machine and then, the two PMMAs were bonded by a solvent assisted thermal bonding. Agrawal et al. proposed a new strategy utilizing two bends of opposite curvature, single sheath inlets and exploiting secondary forces and centrifugal effects for 3D hydrodynamic focusing of dye, particles and cells [97]. A combination of soft- and photolithography was employed to make the mold needed for fabricating the PDMS based microfluidic device and the geometry of the microchannel was optimized for achieving 3D focusing. In another study, Osellame et al. introduced femtosecond laser irradiation as a new fabrication tool for making microfluidic networks that implement hydrodynamic focusing [96]. Basically, femtosecond laser irradiation of a glass substrate followed by chemical etching was employed to make microfluidic device that has only two inlets; one for the sample and one for the sheath flow. 3D printing

27

technology have also been employed to make complex microfluidic devices with less effort, but further research is needed to use 3D printers for making microfluidic devices with desired performance [110]. The majority of reported microfluidic flow cytometers are either too complex or require multiple sheath flows to realize 3D focusing. Despite several studies on simplified designs, further research is needed to make less labor intensive and cost-effective microfluidic flow cytometers capable of efficient 3D hydrodynamic focusing.

In this proof of concept study, we demonstrated a facile strategy for making a microfluidic flow cytometer by using different sized two glass microcapillary pipettes and a glass capillary aligner printed using a 3D printer. Micropipettes have already been introduced to microfluidics; for example, Weitz et al. used micropipettes efficiently for creating monodispersed double-emulsion drops with ultra-thin shells [111, 112]. The fabrication of micropipettes from glass capillaries using a micropuller is quite easy and takes less than one minute and the dimensions of micropipette tip opening can be easily manipulated by either changing the pulling parameters or grinding tip with a microgrinder [113-115]. To the best of our knowledge, this is the first study that shows the utility of micropipettes in efficient 3D hydrodynamic focusing of dye and particles. The proposed fabrication strategy is straightforward, easy and low-cost as it takes less than one dollar to make a new cytometer. Basically, a small sized micropipette is placed inside a large sized micropipette using the glass capillary aligner. The sheath flow is introduced through the large sized micropipette to completely surround and hereby three dimensionally focus the sample fluid coming through the small sized micropipette.

3.2 Materials and Methods

3.2.1 Materials

In this work, utilized materials are as follows: Glass capillary with filament (O.D./I.D.: 1/0.6 mm; length: 90 mm)(Narishige, Japan), blood gas capillary tubes (O.D./I.D.: 2.3/1.85 mm; length: 125 mm) (Marianfeld, Germany), polystyrene microbeads with a diameter of 5.95±0.12 μm (Polysciences, Inc., USA), phosphate-buffered saline (PBS)

(Sigma Aldrich, USA), sealant (Pattex, Henkel, Germany), a high temperature mold material (HTM140 M, EnvisionTEC, USA), a single mode (SM) blue laser illumination fiber (LP405-SF10, Thorlabs, USA), forward scatter (FSC) and side scatter (SSC) fibers (M43L01, Thorlabs, USA).

3.2.2 Device fabrication

First, a small glass capillary tube (O.D./I.D.: 1/0.6 mm; length: 90 mm)was pulled using a micropuller (PC-10 Micropulling Machine, Narishige, Japan) to produce two microneedles with the following parameters; option 2, first-pull position adjustment plate: 6 mm, second-pull position adjustment plate: 2 mm, one type light and one type heavy weights, no. 1 heater level: 65 and no. 2 heater level: 37 [113]. The tip of the small micropipette was grinded to have a tip opening inner diameter of approximately 150 μm using a microgrinder (EG-401, Narishige, Japan) (Fig. 3.1 B$_{II}$).
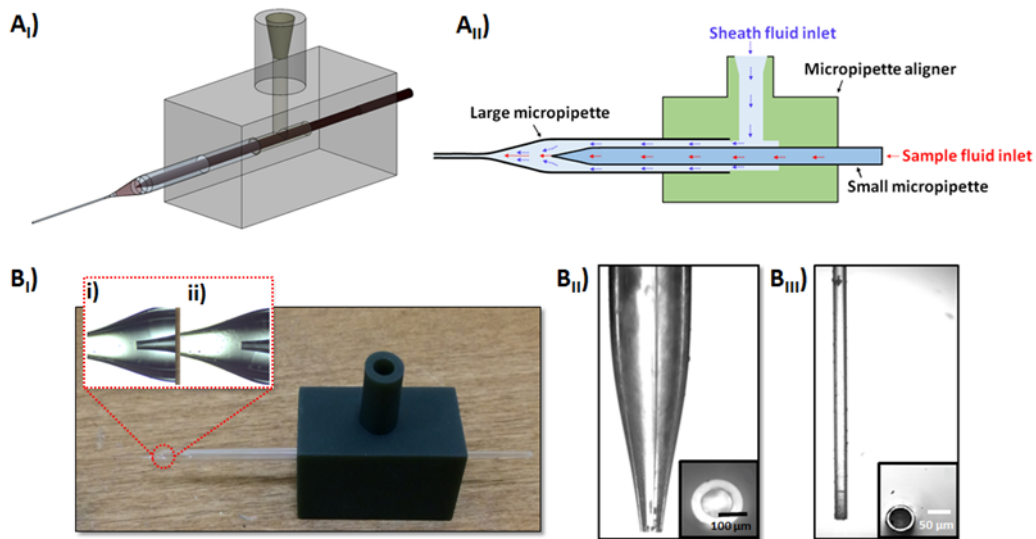
Figure 3.1 : Schematic of the glass micropipette based flow cytometry device (A$_I$) and the principle for hydrodynamic focusing (A$_{II}$). An image of the integrated device with the top (i) and side-view (ii) microscope images of a small micropipette positioned in a large micropipette using the aligner (B$_I$). The optical images of large (B$_{II}$) and small (B$_{III}$) micropipettes.

The desired tip opening diameter was adjusted using the ocular micrometer of the microgrinder. Then, a large glass capillary tube (O.D./I.D.: 2.3/1.85 mm; length: 125

mm) was pulled the same way as the small capillary tube using the following parameters; option 1, two type light and two type heavy weights, no. 1 heater level: 75. The large micropipette was pulled in a way to have a microchannel with an approximately 90 μm inner diameter and a length of no less than 10 cm. The tip of the large micropipette was grinded only to measure the tip opening diameter properly (Fig. 3.1B$_{III}$).

Both micropipettes were cleaned thoroughly in distilled water using ultrasonic before use. The small micropipette was center-positioned inside the large micropipette using a micropipette aligner (Fig. 3.1B$_I$), a process that took only a few minutes. The micropipette aligner was first designed using a 3D CAD design software (SolidWorks 2016, USA) (Fig. 3.2A) and then produced from a high temperature mold material (HTM140 M) using a 3D rapid prototype manufacturing system (Perfactory 4 Mini with ERM, EnvisionTEC, USA) with high precision. As for the assembly of the device, the large micropipette was first inserted in the corresponding hole of the aligner and a sealant was used to both fix the micropipette and prevent any leakage from the small gap between the capillary and the aligner hole. Then, the small micropipette was inserted into the corresponding hole of the aligner to position the small micropipette inside the large one under a stereomicroscope and the same sealant as before was used for micropipette fixation and leakage prevention (Fig. 3.2B). Prior to use, all devices were checked for leakage by pumping water from the two inlets at pressures up to 2 bars, which is the upper limit the pressure pump can provide.
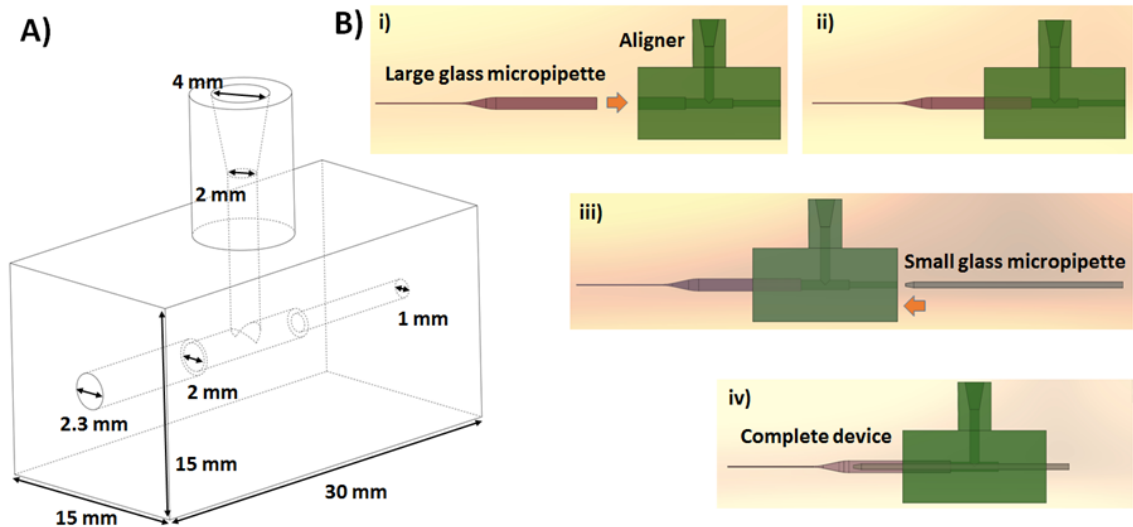
Figure 3.2 : Dimensions of the micropipette aligner (A) and the fabrication steps of the 3D printing assisted microfluidic flow cytometer showing the placement of larger and smaller size glass micropipettes (B).

3.2.3 Device characterization

The 3D hydrodynamic focusing ability of the device was investigated using deionized water (DI) colored with a blue food dye and colorless PBS as sample and sheath solutions, respectively. A pressure pump (Elveflow, OB1) was used to pass the solutions through the micropipettes. In this setting, the PBS solution from the large micropipette hydrodynamically focused the blue color solution introduced from the small micropipette by completely surrounding it (Fig. 3.1A$_{II}$). The impact of the ratio between sheath and sample flow pressures on the 3D hydrodynamic focusing was investigated in a range from 0.96 to 1.064 (sheath / sample flow pressures) (Fig. 3.3A). The 3D hydrodynamic focusing was recorded using a camera (Basler Ace acA2040-90uc, Basler AG, Germany) attached to a microscope (Krüss MSL4000, Germany).
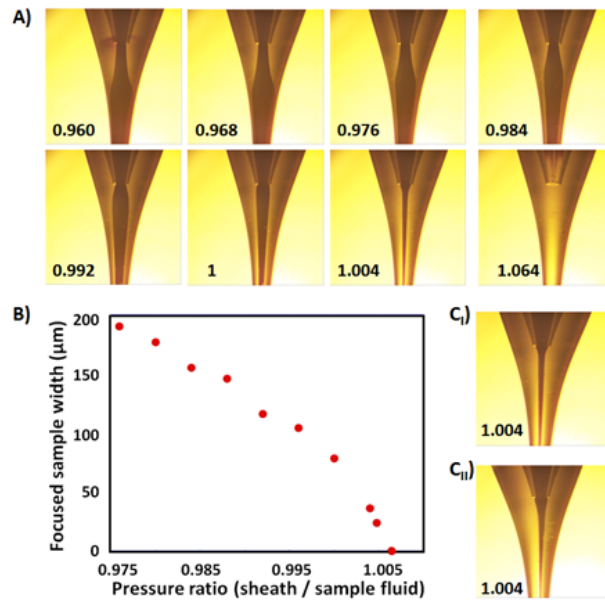
Figure 3.3 : The impact of the varying sheath fluid pressure on the hydrodynamic focusing when the sample fluid pressure is kept constant (pressure of sheath / pressure of sample: 0.960, etc.) (A). Focused sample fluid width vs pressure ratio of sheath and sample fluid (B). The top (C$_I$) and side (C$_{II}$) view of flow.

Next, the device was tested with microparticles of uniform size using an optical test system. The test system consisted of the following components; a single mode (SM) blue laser illumination fiber, forward scatter (FSC) and side scatter (SSC) fibers, two photo diodes (FSC and SSC) (DET02AFC, Thorlabs, USA), a 405nm laser source (LP405-SF10, Thorlabs, USA), a pressure pump and an oscilloscope (Techtronix, MDO3104) (Fig. 3.4 and Fig. 3.5).
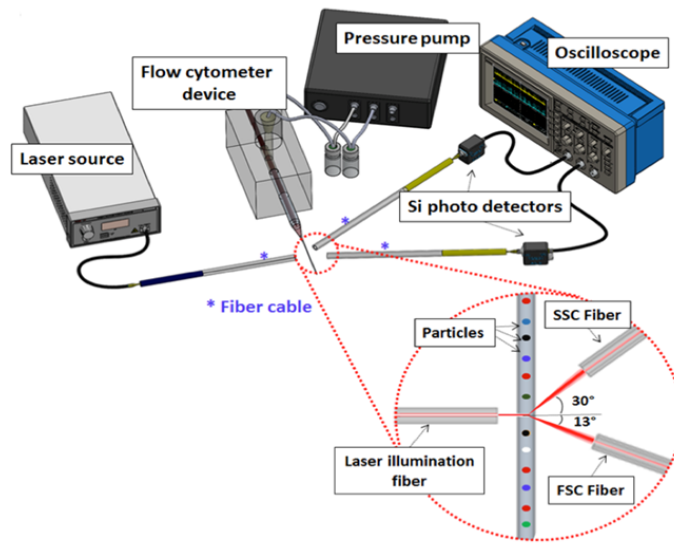
Figure 3.4 : Schematic illustration of the setup used to test the glass micropipette based flow cytometry device

In addition, a flat PMMA plate with fiber guidance grooves was used to position all the fibers (Fig. 3.5B, C). An adhesive tape was used to fix the fibers in the grooves carved on the plate by CO_2 laser (Epilog Zing 30W, Epilog Laser, USA). Basically, the laser illumination fiber with a diameter of 125μm was positioned perpendicular (90°) to the microchannel where the microchannel diameter and the width of the focused sample solution were ~130 and ~18 μm, respectively. The optical fiber with the following specifications (numerical aperture (NA): 0.12, mode field diameter (MFD): 3.6±0.5μm and center wavelength: 405nm) was used to translate a single mode (SM) laser to the interrogation zone where the beam diameter calculated with Gaussian beam approximation is 11.48 μm. To collect the scattered light through the photo detector, FSC and SSC fibers were positioned with angles of 167° and 210° to the laser illumination fiber, respectively. Forward scattered light intensity was reduced via reducing 13° with respect to the 180°. SSC fiber angle was decreased to 210° so as to increase scattered signal intensity. Angular dependence of the scattered light is explained in equation
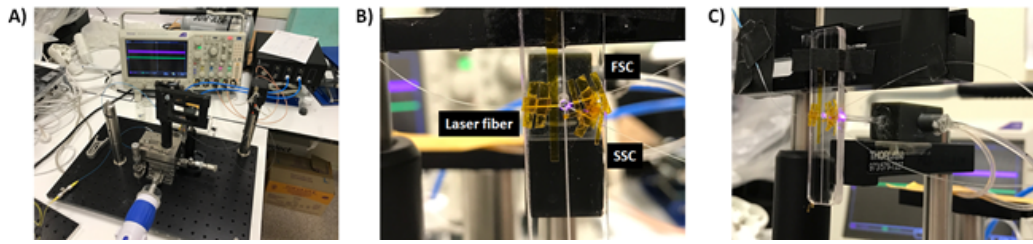
Figure 3.5 : Images of the optical testing system (A), the PMMA plate used for fiber fixation (B) and the microfluidic flow cytometer under test (C).

PBS and polystyrene microbeads containing PBS solutions were used as sheath and sample solutions, respectively. Prior to use, the microparticle (diameter: 5.95±0.12 μm) stock solution was diluted in a mixture (PBS solution + blue food dye) filtered using 0.2 μm pore syringe filter to realize a final concentration of ~1000 particles/μl. The blue color mixture was used simply for better visualization. The microparticle containing suspension was also sonicated for 15 min to minimize aggregation during experiments. Pressure pump was used to pass PBS (sheath) and polystyrene microsphere containing suspension through the large and small micropipettes at a sheath / sample solution pressure ratio of 1.004. The oscilloscope was used to quantify the voltage signals from the photodetectors at a 0.5 MHz sampling rate.

3.3 Result Discussion

The design of the present microfluidic flow cytometer device is quite simple and easily comprehensible (Fig. 3.1A$_{I-II}$). A complete device is composed of three components; a micropipette aligner, a small and a large micropipette (Fig. 3.1B$_I$). Precise fabrication of aligner holes is important for successful micropipette alignment. Manufacturer reports that HTM140 is very durable and high precision material designed to withstand both the heat and pressure of vulcanizing a model in rubber with incredible detail and no loss of dimensional stability. The diameters of small and large holes of different aligners were measured to be 1049.9 ± 8.1 μm (n = 3) and 2303.5 ± 8.9 (n = 3), respectively (Fig. 2.6 A$_{I-II}$). Given the dimensions of the model and the smooth shape of the fabricated holes in Fig. 3.6B, it is safe to say a 3D rapid prototype manufacturing system along with HTM140 material provides dimension accuracy for precise alignment of micropipettes.
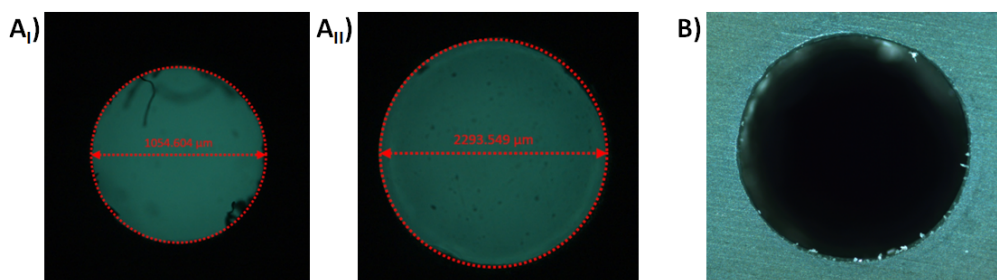
Figure 3.6 : Optical images showing the diameters of small (B_I) and large (B_{II}) holes and the shape (A) of an aligner.

The assembly of the device took less than 10 min including the time needed to grind the tip of the small micropipette. The micropipette aligners can be retrieved easily and used repeatedly for fabrication of a new microfluidic flow cytometer device. The only consumables used to fabricate a new device are the sealant and the glass capillaries, which makes the device ultra-low-cost as both of the consumables cost less than one dollar.

The 3D hydrodynamic focusing ability of the device was demonstrated using deionized water (DI) colored with a blue food dye and phosphate buffer saline (PBS) as sample and sheath solutions, respectively. The different colors of the two solutions made it possible to easily observe the confinement of the sample solution in the microchannel of the large micropipette (Fig. 3.2A). Hydrophilic surface is important for microfluidic systems to achieve various functions such as facilitating fluid flow into microchannels. The water contact angle test result showed that HTM140 is hydrophilic with an average contact angle value of 37.1^O (Fig. 3.7).
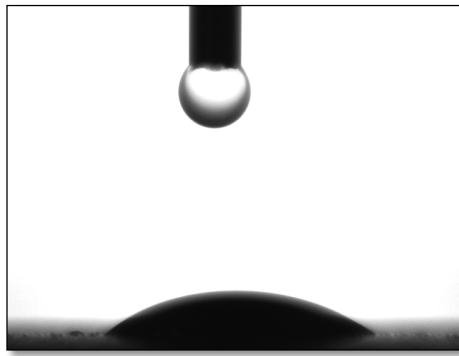
Figure 3.7 : An image showing the result of water contact angle test.

Using the 3D printed micropipette aligner with easy-to-operate two-inlet configuration; the sheath solution completely surrounds and confines the sample solution in a highly efficient manner (Fig 3.1A$_{II}$ − 3.3A). The results showed that the microchannel was filled with the blue color solution at the ratio of 0.96. When the ratio was raised to 1.064, the flow through the small micropipette was blocked by the sheath solution. The small difference between the two ratios demonstrates that the pressure of the two fluids must be controlled precisely for an efficient 3D focusing. The relationship between the width of the hydrodynamically focused sample and the pressure ratio between sheath and sample flows is given in Fig. 3.3B. The width of the sample solution was measured approximately 1.53 mm away from the tip of the small micropipette as shown in Fig. 3.8.
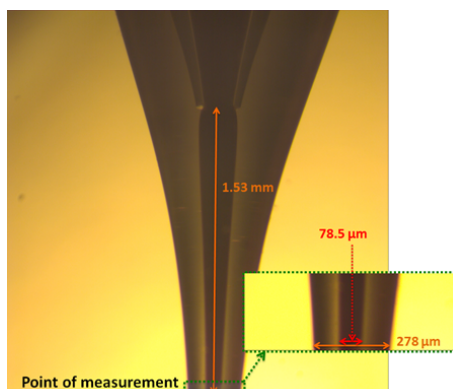
Figure 3.8 : Optical image showing measurement point of focusing test.

The relationship appears to be almost linear, which suggests that the width of the 3D focused sample solution can be precisely controlled by the ratio between sheath and

sample flow pressures. In addition, side view microscope images of the microchannel were taken both horizontally and vertically at a ratio of 1.004 (sheath / sample flow pressure) to see the focused flow and thus verify the 3D hydrodynamic focusing with the present device (Fig. 3.3C). Both images showed that the sample flow was focused close to the center of the microchannel.

Next, the performance of the microfluidic flow cytometer device in 3D hydrodynamic focusing of microparticles was evaluated using an optical test system. Without any particle flow, the FSC and SSC signals show DC offset values due to collecting some amount of light. Fig. 3.9A shows 2-sec FSC and SSC channel signals recorded while microparticles of uniform size were passing through the microfluidic channel. Each peak observed in Fig. 3.9A corresponds to a microparticle passing by the interrogation point. From to the data with ~170 events/s throughput, an FSC peak was recorded for each SSC signal, which indirectly proves that all of the microparticles were focused properly and passed through the laser interrogation region at the same point along the microchannel. Fig. 3.9B shows a close-up view of peak events for 100ms. Since the events were well separated, there is a great possibility to further increase the throughput. The signals were post-processed with MATLAB to obtain the number, peak values and positions of the events. Gating was applied to improve the population distribution with common properties as seen in commercial flow cytometers and to avoid multi-particle events such as aggregated particles.
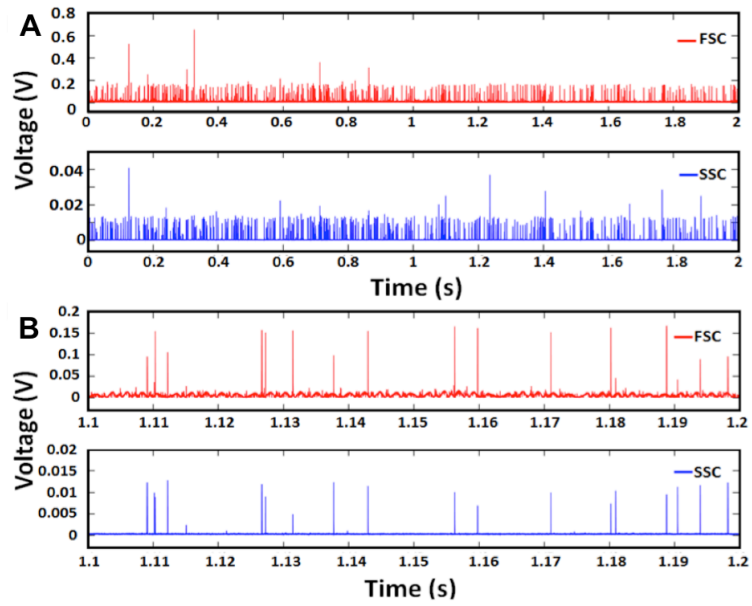
Figure 3.9 : Forward scatter (FSC) and side scatter (SSC) channel signals recorded while passing microparticles of uniform size through the microfluidic channel for 2 seconds with an inset showing 100 ms snapshot.

Fig. 3.10CI and Fig. 3.10CII show the histograms of the peaks observed in FSC and SSC signals given in Fig. 3.9A and Fig.3.9B, respectively. The calculated coefficient of variation (CV) values obtained for FSC and SSC signals were 26.98% and 25.54%, respectively. Lower CV values could be achieved by adjusting the sheath and small solution pressures more precisely [116].
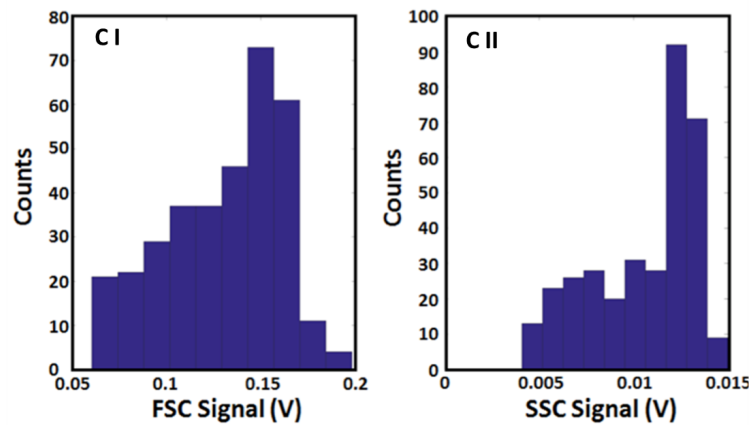
Figure 3.10 : Representative histograms of FSC (CI) and SSC (CII) signals.

38

Accurate alignment of the illumination fiber and FSC/SSC fibers is critical. In this setup, these fibers were aligned using guideline grooves carved on a PMMA substrate by CO_2 laser (Fig. 3.11A$_{I-II}$). In other words, the illumination and FSC/SSC fibers were aligned automatically once they were fixed on the plate using a tape. However, the alignment between these fibers and glass micropipette was done manually using an XYZ stage (Fig. 3.11B, C).
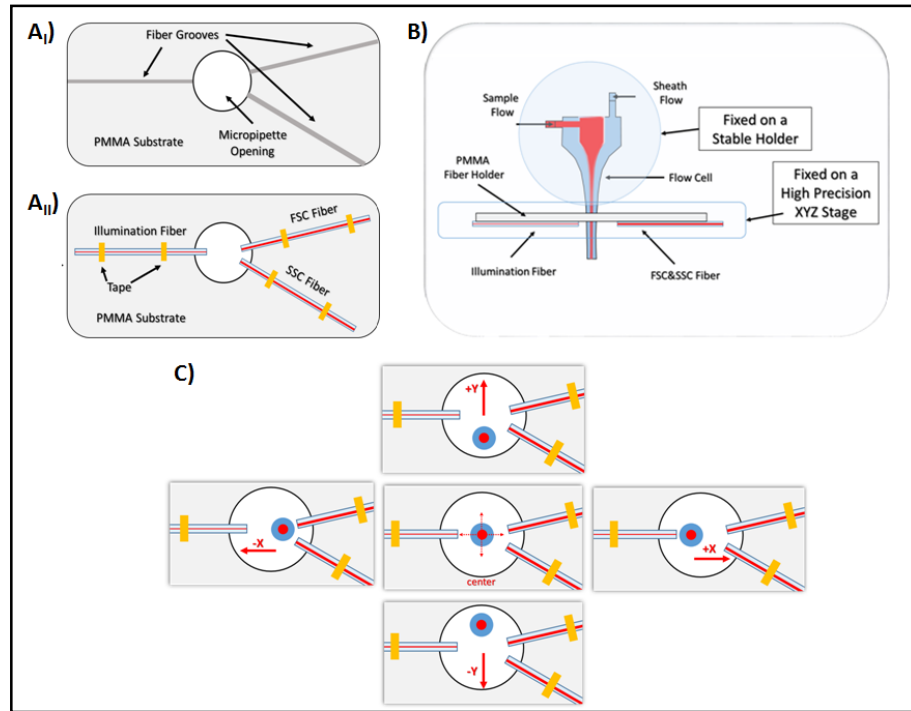
Figure 3.11 : An illustration of the PMMA substrate with fiber guidelines (A$_I$). Fibers are placed and fixed with a tape (A$_{II}$). Fiber holder is connected to XYZ stage to manually adjust the final position (B). An illustration of the move of XYZ stage (and fiber holder) on both x- and y-axis to center the fibers to flow cell (C).

This might be a limitation for the current system as it might take some time for researchers who are not familiar with such instruments. To overcome this limitation, a new strategy will be developed to bypass the manual alignment stage. Basically, a printed apparatus will use to align the whole measurement set up at once. It will be less time consuming and expected to improve the quality of the data. Another limitation of the current setup is sample recovery. This issue will also be addressed in the new

strategy by collecting the outgoing sample in a channel with minimal dilution. A cell sorting mechanism may also be integrated into the system to divert cells of interest.
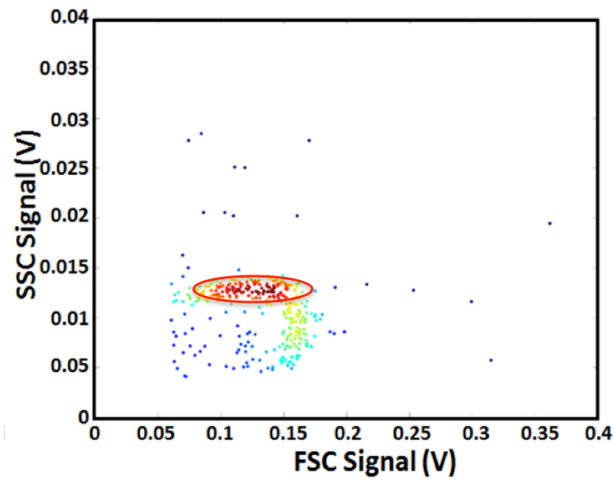
Figure 3.12 : FSC-SSC scatter plot obtained with micro particles of uniform size.

Scatter plot in Fig. 3.12 depicts the correlation between FSC and SSC signals for 2s time duration. It is obvious that most of the events were gathered in a small region, a result that confirms the proper functioning of the device. As compared to commercial state-of-the-art optical flow cytometers, bulk optics (laser diodes, optical lenses, mirrors, filters etc.) and mechanical holders/aligners are excluded from the present setup. The present setup uses fiber optics, which provides great deal of flexibility when considering the integration and stability of optical elements. Unlike benchtop flow cytometers, the flow cell in the present setup is polymer based, which further reduces the cost.

3.4 Conclusion

In conclusion, the fabrication of a low-cost and simple micro flow cytometry device capable of hydrodynamic focusing was demonstrated using different size glass capillaries and a micropipette aligner printed with a 3D rapid prototyping manufacturing system. The assembly of the device took less than 10 min including micropipette tip grinding and the final device is ultra-low cost. The device showed an excellent performance in hydrodynamic focusing of DI water colored with a blue food dye. The device was also used for 3D hydrodynamic focusing of microparticles of uniform size

40

where distinct FSC and SSC signals of microparticles passing through the optical interrogation point were successfully recorded. Given the separation between each event, the device has the potential for further increase in throughput. The device offers simplicity, low-cost and good performance in hydrodynamic focusing and has a great potential to be used in a wide range of flow cytometry applications.

4. COLORIMETRIC BISPHENOL A DETECTION WITH A PORTABLE SMARTPHONE-BASED SPECTROMETER

4.1 Introduction

The detection of health-damaging chemicals and compounds in aqueous media has drawn a great interest to ensure public health protection. Bisphenol A (4,4'-(propane-2, 2-diyl)diphenol, BPA) is one of the most well-known endocrine disrupting compounds [117]. Due to the presence of phenol groups on the structure, BPA has binding tendency to the estrogen receptors, and it change or cease endocrine functions within body [118, 119]. Even low exposure levels are identified with infertility, obesity, diabetes, thyroid malfunction, prostate cancer, breast cancer, attention deficit disorder [120-123]. Despite being a toxic organic compound, BPA is the most common synthetic compound utilized in plastic industry as a monomer [124, 125]. It affects indirectly public health as contaminated plastic utensils, water bottles or food containers [126, 127], since previous studies showed that BPA can migrate from these plastic materials into food and beverages. Accordingly, BPA accumulation in human body is the main reason of increasing cancer rates and autoimmune diseases [128, 129]. Eventually, the development of field deployable, cost effective, and highly accurate detection methods are needed to monitor exposure levels of BPA in the environment, food and human body.

Up to now, numerous analytical methods for the analysis of BPA have been employed such as high-performance liquid chromatography system with ultraviolet (HPLC─UV), HPLC─mass spectrometry (MS), gas chromatography (GC─MS), fluorescence and electrochemical detection [11-14]. Although these methods can provide accurate and precise results, they mostly require complex instruments located in central laboratories with access to specialist labor. Recently, enzyme-linked immunosorbent assays (ELISA), chemiluminescence immunoassay, molecular imprinting-based detection approaches, nucleic acid-based aptamers, and electrochemical methods have been developed [130-134]. Among them, electrochemical sensing is a widely accepted

technique with high sensitivity and simplicity for the detection of BPA. It is well known that BPA possesses electrochemical activity due to its electrochemical-active phenolic hydroxyl groups that can be oxidized. The electrochemical characteristics of BPA have been examined at different electrode materials such as carbon and metals [135, 136]. However, the relatively high potential requirement for the oxidation of phenolic compounds results in a decreased sensitivity due to the increase in background current. Various approaches including the use of enzymes and surface modification of the electrode have been proposed to reduce this disadvantage. Carbon nanotube [137-139], graphene [134, 136, 140-145], quantum-dot [145, 146], metal composite [135, 147, 148], and nanocomposite based [149-151] sensors have been developed to improve the electrochemical reactivity of electrodes. For example, Ma *et al.* have fabricated an electrochemical impedance aptasensor performing in a range of femtomolar detection limit, in which gold nanoparticle coated boron doped-diamond was modified with aptamer [152]. However, difficulties in efficient and repeatable sensing of BPA have been reported [153, 154] due to weak electroactivity and deposition of oxidation on the electrode surface.

Over the last decade, cameras are widely used in quantification of color images within the colorimetric and photometric methods in scientific domains. Sumriddetchkajorn et al. reported one of the pioneering works where a webcam 2D image sensor was used as spectrometer sensor and numerous fiber optic cables were used for signal translation to the sensor [155]. Advancements in 3D printing technology and camera marketing let smartphones become an infrastructure for scientific researches [156]. Zhu et al. reported a smartphone based optofluidic fluorescent imaging cytometry and achieved to read a few micro range bead detection [29] and Talukder et al. reported smartphone integrated microfluidic impedance cytometer [157]. Additionally, previous studies reported direct quantification of colors from test strips or solutions by using a mobile device. This mobile-platform based colorimeters were used for monitoring chlorine concentration in water [158, 159], estimating nitrogen in rice leaf [160], quantifying peroxide content [161], the detection of saliva alcohol [162], biomarkers in sweat and saliva [163], urine [74, 164], pH and/or nitrite [165]. Recently, we have proposed smartphone spectrometer

for investigation of methylene blue dye adsorption from water demonstrating the effect of fiber size on the spatial and spectral resolution [166]. Another smartphone-based sensing study has been reported by McCracken *et al.* with the detection limit of BPA in micromolar range and LED flash has been used to stimulate the fluorescence molecules [167].

Camera and sensor advances together with the increasing capability in computer processing have led to emergence of more portable, cost-efficient and user-friendly platforms to quantify and analyze the particular content of the assays/solutions. One method is to use color information which changes with the concentration (Peroxide amount [161] or time (methylene blue degradation [166]) depends on the application. After images are captured for each distinct condition, features are extracted to train the system (machine learning or neural network systems) that can then automatically perform colorimetric tests as new data arrives. This method can be used both solid samples like paper-based test and liquid samples like colored solutions. For liquids, besides this approach, spectral data can also be used as an alternative. Spectral data (derived by spectroscopic instruments like UV-Vis, FTIR, NIR and chromatographic instruments like HPLC, GC) specify variables with its properties and provide useful information about the molecules. With the use of spectral data, chemical composition of the materials can be identified. Therefore, spectrometers are used commonly in laboratories and scientific fields such as chemistry and biology as well as in many industries such as forensic, printing, and more. Our aim is to combine the aforementioned spectral data with the widely used spectrometer under the smartphone technology to reveal a portable and cost-effective design.

In the present study, we have developed an ultra-low cost, portable, plastic fiber based smartphone spectrometer with a custom designed immersion probe and a cradle for rapid and sensitive detection of BPA in distilled, commercial and tap water samples. The colorimetric assay based on the formation of quinone-type complex in alkaline medium has been conducted. The smartphone system has been turned into a visible spectrometer system to accommodate absorbance measurements in BPA mediated solutions using the

44

reflective probe. The proposed reflection based smartphone spectrometer is straightforward, robust and could facilitate remodeling the science of measurement for health disrupting agents.

4.2 Material Method

4.2.1 Portable smartphone-based design

The custom design of the 3D printed components smartphone based spectrometer is shown in Fig 4.1a. LG G4 (South Korea) smartphone rear-facing camera was used as detector with the specifications of 1/2.6 inch sensor size, 5312x2988 pixel resolution, and 1.12 μm pixel size. Smartphone cradle, body alignment part, diffraction grating holder and the immersion probe were all custom designed and fabricated using a 3D printer (Zortrax M200) consuming of ~100g Acrylonitrile Butadiene Styrene polymer. Smartphone cradle and body alignment part includes hot-plug tracks for easy alignments. Also, grating holder is designed as pluggable and carries groves for the grating to firmly position. Body alignment part success the alignment of collecting fiber and transmission diffraction grating (1000 lines per mm, Rainbow Symphony). Collecting fiber that collects reflected radiations from probe is positioned with the degree of 42° to the normal of the grating so as to drop first order-diffracted light spectrum (m=1) on the camera. Therefore, the distance is arranged as 11.7 mm between grating and camera. Smartphone flashlight is fiber coupled to the immersion probe and then the reflected radiation is coupled to the camera via passing though grating. Here the probe is developed using on a plastic (PMMA) based bifurcated fiber bundle with the diameter of 0.5 mm (also known as Y-cable) and it includes fine polished stainless steel (3 mm in thickness, UNS S31600, AK Steel Corporation). The distance between the bifurcated optical fibers and the steel surface is 16.5 mm. The immersion probe is shown in Fig. 4.1b. Total cost of reflection based smartphone spectrometer system consisting plastic fibers, diffraction grating, metal surface at the bottom of the probe, and 3D printed parts is less than $5 except smartphone. Fig. 4.1c shows overall smartphone based spectrometer system which does not include any additional optical components.

The spectral images of blank solution (the left image) and 5 ppm BPA solution (the right image) were given in Fig. 4.1d, indicating the color intensity variation in different concentrations.
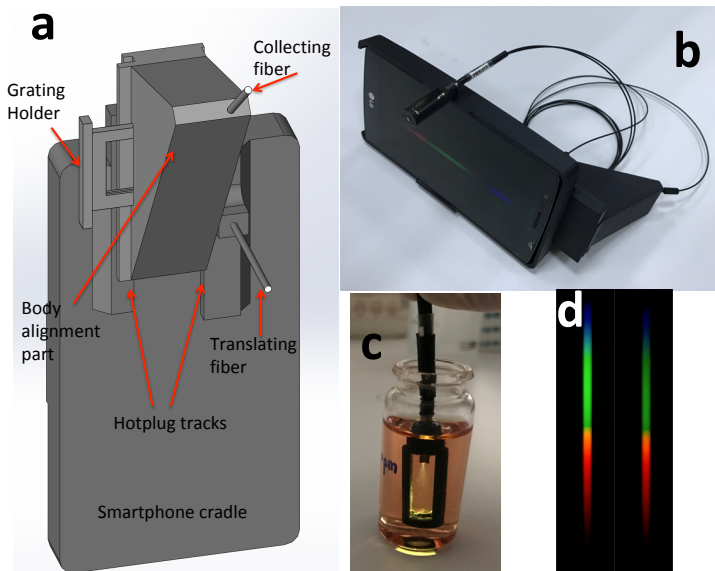
Figure 4.1 : (a) 3D printed components of smartphone based spectrometer, (b) completed form of the smartphone spectrometer with a plastic immersion probe, (c) the probe immersed into an analyte solution, (d) Representative spectral images from smartphone spectrometer.

4.2.2 Image processing

A digital camera captures an image using an array of millions of tiny pixels that are sensitive to light. Pixel intensity value is directly related to the number of photons received by each pixel. Since pixels are incapable of distinguishing the photons with respect to color, only grayscale images can be created in this way. Color images are created by covering neighboring pixels with the color filter array that permits only one of three primary colors such as red (R), green (G) or blue (B). This means each pixel has only one color information, which leads to a generation of RAW image. Demosaicing method, interpolation of two known color from the neighbors, is used to estimate the other two color values of the pixel. After this step, the RAW image becomes viewable on the screen. To obtain more appealing images, post-processing methods such as white-

balance, gamma correction, color space correction, and compression are performed, which eventually leads to a commonly used format like JPEG.

JPEG images have certain advantages over RAW images such as small memory to store and being instantly displayable. However, some issues arise from this conversion such as non-linear RGB color space [55], data loss due to the compression and having only an eight-bit color depth. On the other hand, RAW images are free from post-processing which means they include original image data with 10-14 bits color depth. The post-processing methods cause corruption in linearity of the image. In RAW images, the relation between the intensity value and the number of photons in the pixel is linear which is necessary for quantitative scientific data acquisition.

In this study, all the images were taken and processed in RAW format to avoid the limitations of JPEG format. Also, raw data allow for more precise image analysis. There are three RAW file formats to work. Nikon cameras produce RAW image with ".NEF" extension while Canon creates image with ".CR2" extension. Here, ".DNG" raw file format, developed by Adobe Company, was studied because it is released as an open format and widely employed compared to ".NEF" and ".CR2". The images were transferred to a computer to process in MATLAB after capturing with smartphone since processing raw images require high computational power. Firstly, reliability of the camera was tested using five consecutive images captured in JPEG format. After the intensity values were normalized, the deviation was found ±2.73%. Hence, it was found to be adequate to use average of five consecutive images in order to enhance the reliability of the results. Also, all parameters like shutter speed and ISO were kept same to capture the images under same conditions, and the manual mode was employed to avoid possible post-processing operations than could be performed by the smartphone. The images in ".DNG" format were then converted to tagged image file format (TIFF) for easier extraction of the red (R), green (G) and blue (B) values with DCRAW software [56] which maintains the linear relationship between RAW images and the radiance scene. After that, RGB values of the images were converted to HSV (Hue–Saturation–Value) to reduce the effect of illumination change. The V (Value) was used

in further processing steps of the images to quantify the amount of the transmitted light through the solution for this study. The image processing pipeline is depicted in Fig. 4.2a which summarizes the overall process in four steps. To calculate corresponding wavelength value of each pixel, a calibrated fiber-optic spectrometer (HR2000; Ocean Optics, FL, USA) was used. The calibration method [57] assumes that the wavelength value and pixel index have a linear relationship and the peak locations in the visible wavelength range for a fluorescent light source and distances between them were used to extract the linear equation to convert from pixel index to nanometers. As illustrated in Fig. 4.2b, after the smartphone spectrometer was calibrated successfully with a dispersion value of 0.248 nm/pixel, these peaks overlap completely.
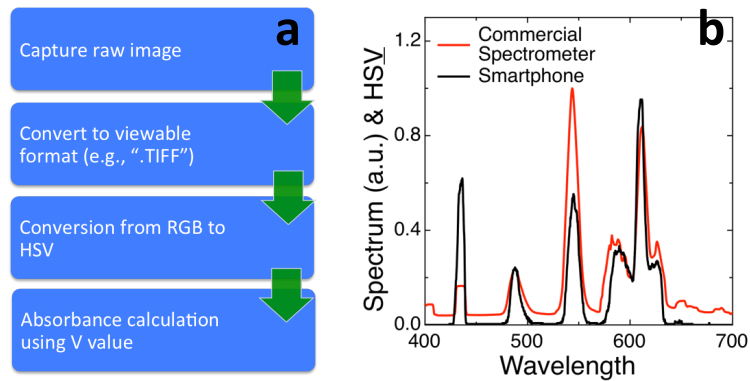
Figure 4.2 : (a) Image processing steps for the conversion of raw image into absorbance data, (b) The output spectra from commercial and smartphone spectrometers for calibration process.

The calibration method [41] assumes that the wavelength value and pixel index have a linear relationship including extracted spectral resolution values for different size plastic fibers. In Fig. 4.2b, smartphone spectrometer was calibrated with the commercial spectrometer and a dispersion value of 0.248 nm/pixel was found for 0.5 mm fiber optic cable. There are four peaks between 400 nm and 700 nm for smartphone and commercial spectrometers due to the fluorescent nature of the light. As illustrated in Fig.4.2b, these peaks need to be overlapped after the calibration operation is performed successfully.

4.2.3 Detection of bisphenol A in aqueous media

Bisphenol A (BPA) (Sigma-Aldrich, ≥99%), 4-Aminoantipyrine (4-AAP) (Sigma-Aldrich, >98%), potassium ferricyanide (Carlo Erba), sodium bicarbonate (Sigma-Aldrich, ≤99.7%) were analytical grade and used as received without further purification. The concentration of the phenolic compound was determined by a colorimetric reaction with 4-AAP and potassium ferricyanide [42]. A stock solution of BPA (200 ppm) was prepared in ethanol; subsequently diluted to the concentrations ranging from 0.1 to 10.0 ppm. The pH of BPA solutions was adjusted to 8.0 using 0.25M NaHCO3 and distilled water. 1.5 mL of 20.8 mM 4-AAP and 1.5 mL of 83.4 mM potassium ferricyanide solutions were consecutively added to 12 mL of BPA solutions. After 10 min incubation, the solution absorbance was measured using a smartphone based spectrometer system and a calibrated spectrometer. The absorbance value was read at 506 nm and the BPA concentration was determined from a standard curve. The effect of pH on the detection of BPA (10 ppm) was conducted after adjusting the initial pH levels of the solutions to 7.0, 8.0, 9.0, and 10.0 using 0.25M $NaHCO_3$, NaOH and HCl solutions. To evaluate the accuracy of the proposed method, an accurate determination of BPA in commercial drinking water was obtained by the standard addition method at pH 8.0 both with a smartphone based spectrometer system and a calibrated spectrometer.

4.3 Results and Discussion

BPA concentrations were measured using a colorimetric assay described by Emerson [43]. The use of Emerson's reaction offers many advantages such as speedy results, ease of manipulation, the use of relatively stable reagents, and applicability over a wide range of concentrations of phenolic material [44]. Under alkaline environment when a phenolic solution is reacted with 4-AAP in a presence of potassium ferricyanide as an oxidant, the colored complex is formed. The primary amine of 4-AAP exerts an electrophilic attack on the para-position of an oxidized phenol forming a quinone-type complex. Maximum wavelength for BPA after completion of the reaction was reported

as 506 nm [42]. The absorbance of BPA solutions at different concentrations with absorption maximum at 506 nm was measured by both smartphone and commercial spectrometers. BPA solutions were prepared as 0.1, 0.2, 1.0, 2.0, 3.0, 4.0 and 5.0 ppm and the final pH values were adjusted to 8.0. Fig. 4.3a shows the color change of the solutions, which turns gradually from yellow to orange with respect to the increase in BPA concentration. To obtain the absorbance spectrum, the multicolored images from smartphone were processed and the value of absorbance was calculated using Beer-Lambert Law. Proportionality in the absorbance with the initial concentration of BPA in the assay was observed. Fig. 4.3b shows a comparison of the spectra obtained by the smartphone and commercial spectrometer. The related calibration curves for the BPA solutions are shown in Fig. 4.3c, with coefficient of determination values (R^2) of 0.996 and 0.977, respectively. The possible reason for the small shift in absorptivity may be due to internal filters of smartphone camera and non-linear responsivity of the sensor [166]. The calibration curves indicate a limit of detection (LOD) of 0.285 ppm and 0.232 ppm for the smartphone and commercial spectrometer, respectively. The sensitivity of the smartphone spectrometer system was found to be 0.101/ppm. The dynamic range of the sensing system varies between $0.285 - 5.000$ppm. The inset graph magnifies the concentration range between 0-1 ppm. Here, the negative absorbance was observed in low concentration values (smaller than 0.2 ppm) as the negative absorbance values arise from measurements higher than the blank measurement. These measurements are below the LOD and are more likely to noise due to CMOS imager on smartphone. The number of blank measurements could bring the absorbance values close to 0, leads to signal to noise ratio improvement. Having similar results with commercial spectrometer also proves that low analyte levels are prone to measurement errors.
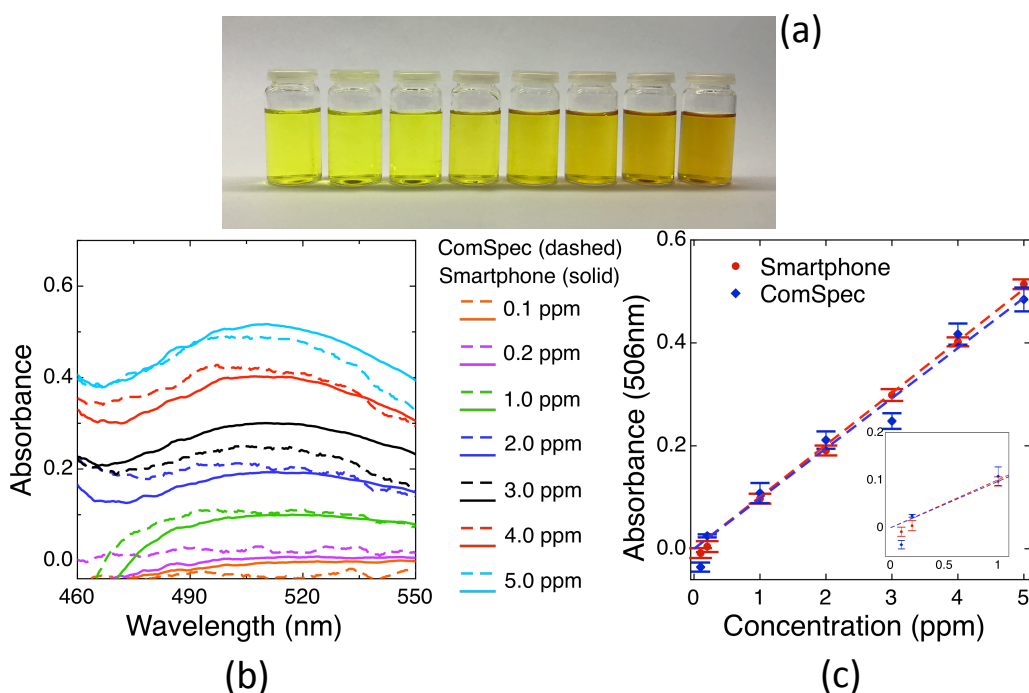
Figure 4.3 : (a) BPA solutions from 0 to 5.0 ppm. (b) Absorbance spectra obtained from smartphone and commercial spectrometers for the serial dilutions. (c) The absorbance at 506 nm was measured by smartphone and commercial spectrometers. (The inset shows the enlargement of curve at low concentrations ranging from 0 to 1.0 ppm.)

McCracken et al. reported smartphone-based fluorescence detection of BPA via 8-hydroxypyrene-1,3,6-trisulfonic acid (HPTS) as a fluorescent probe. They determined BPA with a detection limit of 1.0 ppm in waste leachate and industrial samples using fluorescence spectroscopy and iPhone 5S or Nexus 5X standalone sensor platforms [54]. Compared to the previous report on smartphone-based detection of BPA, the proposed cellphone based devices performed lower limit of detection.

Emerson and Kelley suggested that pH is an important variable in the quantitative application of Emerson's reaction [61]. It is well established that this colorimetric reaction should be carried out in a controlled pH conditions. Under acidic pH values, the reaction between the phenolic material and 4-AAP leads to the formation of antipyrine red [61]. On the other hand, under alkaline conditions, the complex between phenolic material and 4-AAP, which form the basis of this method, is stronger. Similar

observation has been reported by Gottlieb and Marsh [62]. They noted that the most suitable pH was 10.4-10.6 for 2,2'-methylenebis[4-chlorophenol] and 4-AAP. Therefore, the effect of pH was studied in solutions containing 10 ppm BPA. Photographs of BPA solutions with pH values of 7.0, 8.0, and 10.0 were demonstrated in Fig. 4.4a. The images on the left show blank solutions and on the right show analyte solutions at 10 ppm. As expected, 4-AAP forms a stable orange-colored complex with BPA and exhibits a yellow color in the absence of the analyte under alkaline conditions. However, at pH 7.0, blank solution has completely different color, and a nonstable colored complex form which is also observed below pH 7.0. Fig. 4.4b shows the corresponding absorbance values of BPA solutions at different pH values obtained from smartphone and commercial spectrometers.
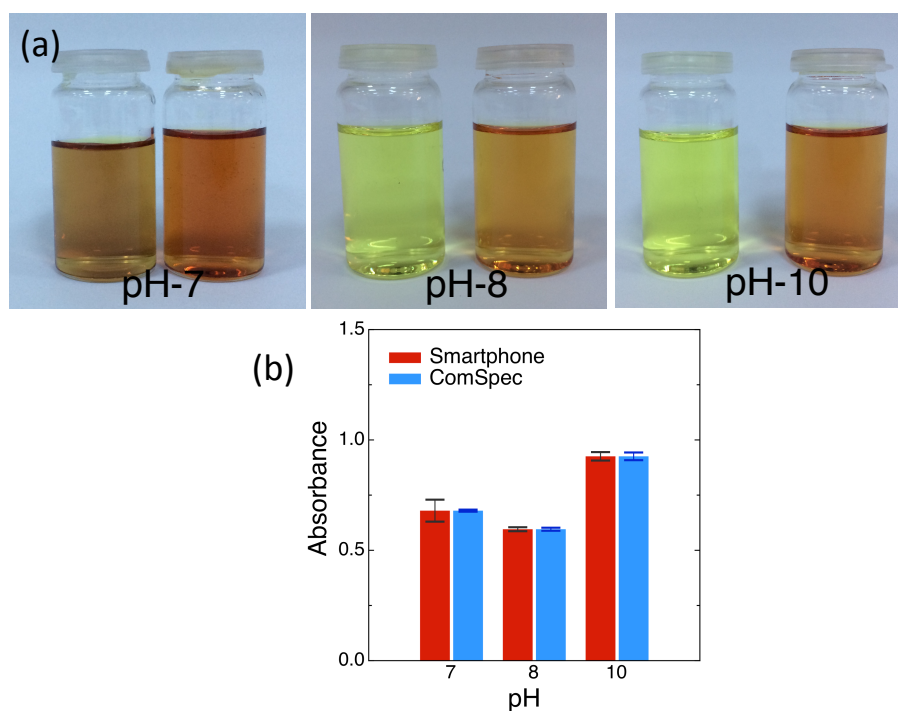
Figure 4.4 : a) BPA solutions at different pH values, b) Effect of pH on the absorbance of BPA solutions measured using smartphone and commercial spectrometers.

We can draw two conclusions from the results described here. The first is that smartphone-based colorimetric assay can conveniently be performed above pH 7.0. The second is, with the exception of pH 7.0, higher absorbance values were obtained by commercial spectrometer compared to the smartphone spectrometer. This can also be

attributed to different absorptivity values obtained from calibration curves, which concludes that same smartphone should be used to study the absorptivity of the analyte. To demonstrate the potential application of this technique in an analysis of real sample, the smartphone spectrometer was tested on the commercial drinking water by standard addition method at pH 8.0. Fig. 4.5 shows a comparison of absorbance intensities of spiked BPA in commercial water using smartphone and commercial spectrometers.
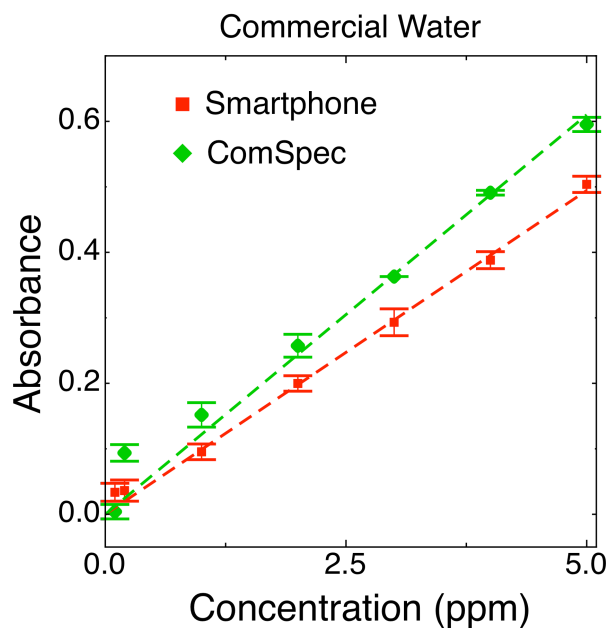
Figure 4.5 : Comparison of absorbance intensities of spiked BPA in commercial water samples using smartphone and commercial spectrometers.

Here, two lines are separated from each other by the concentration level while they are almost overlapping in Fig. 4.3c. The common ion effect is most encountered reason for the noticeable separation observed in commercial water which contains several types of interfering ions compared to the distilled water. Therefore, the stability of complex formation is negatively affected by the increased number ions, resulting in deviation between the two curves. Moreover, a detection limit of 0.64 ± 0.014 ppm was obtained in commercial water using the smartphone spectrometer while it was found as 0.55 ± 0.011 ppm using the commercial spectrometer. The BPA concentrations show relatively similar characteristics, indicating that the performance of the smartphone spectrometer is comparable to the commercial spectrometer. Our results prove that the

proposed smartphone spectrometer can readily be used for rapid detection of BPA in water samples under controlled pH conditions.

4.4 Conclusion

A rapid quantification of BPA was reliably performed by colorimetric analysis in water samples with the help of a reflection-based smartphone-sensing platform with plastic immersion probe. This colorimetric system provides detection of BPA in the dynamic range of 0.29 — 5.0 ppm under alkaline pH conditions. The detection limit of the system was found as 0.29 ppm with the sensitivity of 0.1/ppm. The findings of this study suggest that the smartphone spectrometer, successfully recognizing chemicals with a low limit of detection, is capable of subrogating benchtop spectrometers. As a consequence, our approach opens the door toward the portable micropollutant monitoring which can be extended to smartphone-based point-of-care diagnostics and environmental analysis.

5. DEVELOPMENT AND APPLICATION OF A LOW-COST SMARTPHONE-BASED TURBIDIMETER USING SCATTERED LIGHT

5.1 Introduction

Turbidity is a commonly used water quality parameter that indicates the clarity of water. It is an optical characteristic of water and a function of the amount of light scattered by the suspended particles in water. Thus, waters with high turbidity has low visibility and clearness. Turbidity is typically caused by organic and inorganic suspended materials that originate from natural and/or anthropogenic sources [168]. Clay, silt, fine sand, organic matter, algae and other microscopic organisms can cause turbidity in water. Typically, high turbidity waters represent lower water quality and is considered to be aesthetically unappealing [169]. Although, turbidity doesn't represent an indicator of public health risk, it can make someone percieved about presence of pathogenic microorganisms and known as a strong evidence of hazardous events on the water supply system. In essence, turbidity is an inherent indicator of environmental and public health.

Turbidity can be measured in a number of different ways including (i) simple visual methods and (ii) instrumental methods. Commonly used visual measurements are done by Jackson Candle Turbidimeter and the Secchi Disk whereas instrumental methods are based on the optical principles of nephelometry and spectrophotometry [170]. The nephelometric method is the standard turbidity measurement technique that essentially measures the cloudiness of water by using the light scattering character of particles found in water. In this method, turbidity is considered to be high when the amount of light scattered is high. The scattered light captured by a detector is compared with the incident light and the result is represented by nephelometric turbidity unit (NTU) [171]. The spectrophotometric method, on the other hand, is based on the principle of measuring the transmitted light rather than scattered light and recording the absorbance of light at different wavelengths. While visual methods are direct measurement

techniques, instrumental methods use indirect techniques that require known standard solutions and calibration to correlate measured optical response to turbidity.

The measurement of turbidity in the field is an important asset for water quality monitoring programs. The low cost visual methods can provide rapid and low-cost determination of turbidity at the cost of accuracy. The more sophisticated optical methods are accurate but require costly equipment and often require laboratory measurements [172]. Based on this premise, there is a need for an accurate but low-cost measurement procedure that does not require too much labor under field conditions. In this regard, smartphones can provide a valuable tool for accurate, fast and low-cost measurements of water quality under field conditions. They can be quite effective in screening level monitoring campaigns where the decision to include the measured point in the program needs to be made instantaneously.

Smartphones were able to achieve environmental and health monitoring via detecting fluoride [173, 174], chlorine [159]and water salinity levels [175], pH [176, 177] and waterborne pathogens [178-180]. Recently, using the ambient light sensor of a smartphone, water turbidity levels as low as 0.1 NTU was measured using a compact design with external infrared LED source [181]. Consequently, this study presents the results of an ultra-low-cost, portable smartphone turbidimeter based on spectroscopic measurements of both forward and side scattered light. The proposed instrumentation requires no active electrical or optical components and only uses smartphone's own sensors and software. The two measurement modes of the smartphone turbidimeter provide an accurate and practical methodology for field measurement of turbidity.

5.2 Materials and Methods

5.2.1 Smartphone turbidimeter

The proposed smartphone turbidimeter design was fabricated using a smartphone (LG G4, 1/2.6" sensor size with 5312x2988 resolution, 1.12μm pixel size) and a 3D printed cradle as shown in Fig 5.1a. The compact design includes a stand and a diffraction grating attachment for the smartphone, turbidity vial holder and plastic fibers for light

delivery and collection. All plastic parts were fabricated using Acrylonitrile Butadiene Styrene (ABS) polymer printed on 3D printer (Zortrax M200) using ~200g of material except plastic fibers that are PMMA. Working principle of smartphone turbidimeter is shown in Fig 5.1b. Basically, the light source, LED flash of the smartphone, was brought to the turbid medium using a 1.5 mm plastic (PMMA) input fiber. After interaction with suspended particles in the medium the forward scattered (FSL) and side scattered light (SSL) were collected using perpendicularly located 0.25mm and 1.0mm fibers respectively. Both FSL and SSL pass through a diffraction grating located 42° to the normal and produce a dual spectral image on the camera sensor. Depending on the fiber size (0.25 vs. 1.0mm), the spatial resolution of the spectral image changes, i.e. the visible spectrum on the smartphone in Fig. 5.1a.
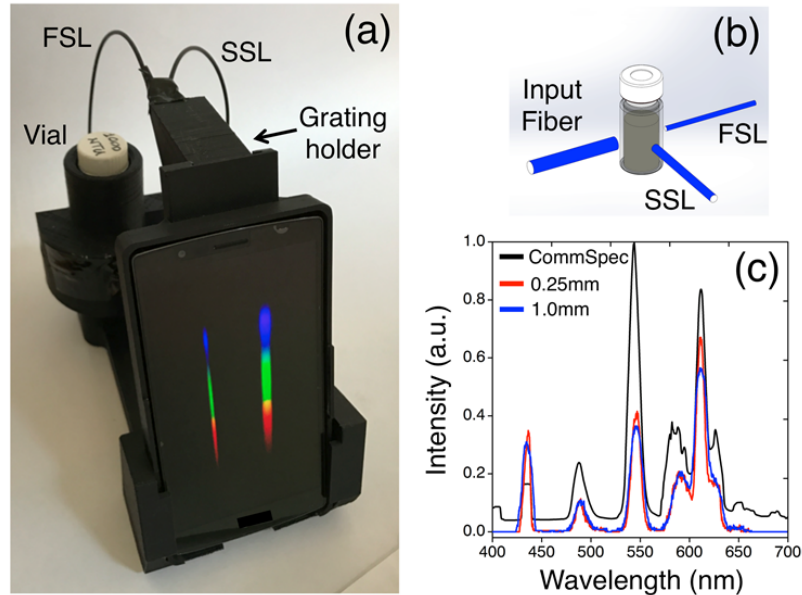
Figure 5.1 : a) The fabricated smartphone turbidimeter with a stand, vial holder, grating holder and plastic optical fibers, b) The light is launched using an input fiber and scattered light is collected via FSL and SSL fibers, c) The calibration of the smartphone spectrometer using a commercial spectrometer.

The smartphone camera was used in Manual Mode for both FSL and SSL measurements, and shutter speed, ISO level, focus level and white balance was all kept constant during the experiments. The distance between the grating and camera is ~11 mm, and only the 1st order diffraction pattern was projected on the camera. The

smartphone turbidimeter does not include any other optical components and it is straightforward to assemble the entire setup. All parts are mechanically aligned after assembly and the total cost of the system is calculated to be less than $10.

The conversion of the pixel index to wavelength was done with the help of a calibrated commercial spectrometer (HR2000; Ocean Optics, FL, USA). The fluorescent lamp spectrum with unique peaks and the distances in-between were used as the calibration spectrum and a linear equation was constructed to convert pixel indices to nanometers. Instead of red-green-blue RGB values of an individual pixel, the value of the Hue-Saturation-Value (HSV) color space was used to represent the light intensity of the spectrum. Furthermore, instead of using the pixel values of a JPEG image, we processed the RAW image that is more suitable for scientific data acquisition [15, 16]. RAW images offer better color depth (12 vs. 8 bits) over JPEG images and the pixel intensity is linearly related to light intensity. RAW images are unprocessed and are not subject to post-processing methods such as white balance, gamma correction, color space addition, and compression to reduce the size. Accordingly, the RAW images obtained in ".DNG" format were transferred to a computer to process using MATLAB and DCRAW software [17] and pixel values were quantified. The final fluorescent light spectrum using 0.25 and 1.0mm fibers on the smartphone and the commercial spectrometer system is demonstrated in Fig. 5.1c. The linear dispersion ($d\lambda/dl$) value was found to be 0.253 nm/pixel.

5.2.2 Turbidity units (NTU) calculation using SSL

In nephelometric measurements, the light source and photodetector are placed 90° with respect to each other. Accurate nephelometric measurements are limited to 0-40 NTU range because of the relationship between light scattering and turbidity. In this range, scattered light and turbidity have a linear relationship [162, 182] and beyond this range, this linearity is lost.

Nephelometric turbidity is based on the following equation,

$$T = a_0 x \, I_{90} \tag{5.1}$$

where T is turbidity in NTU units, a_0 is the calibration constant and I_{90} is the 90° detector current.

The amount of total suspended solids in a turbid medium and the photodetector current are linearly related. In our case, the photodetector signal (i.e. detector current) is analogous to the change in SSL, which is the 90° detection signal obtained spectrometrically. As in the case of nephelometric instrumentation, a dark signal for the photodetector was obtained with a 0 NTU distilled water solution and was used as the baseline for detection. Since the smartphone turbidimeter does not have any active detector component, the change in V from HSV color space for a specific wavelength was used for linear fitting in the 0-40 NTU range.

5.2.3 Turbidity calculation using FSL

Suspended particles in the light path reduce the light intensity via absorption and scattering. As in the absorbance spectroscopy technique, FSL intensity was used to calculate the absorbance as a function of wavelength. Then, the Beer-Lambert law, that originally relates the absorbance (A) and concentration of a liquid, was used to extract turbidity in units of NTU. In the following equation,

$$A = \log (I_0/I) \tag{5.2}$$

where I_0 is the FSL intensity for 0 NTU distilled water at a specific wavelength, and I is the intensity for higher turbidities. Once the characteristic equation between absorbance and turbidity is obtained, it is used to estimate the turbid nature of unknown solutions in the 0-40 NTU range.

5.2.4 Material preparation

In order to calibrate the SSL signal, the Formazin standard solutions (Bereket Chemistry, Turkey) were tested with a calibrated nephelometric turbidimeter (Hach 2100P). The NTU values of the formazin standards range from 0.43 ± 0.07 to 982.8 ± 4.32

NTU as listed in Table 5.1. Figure 5.2a shows the standard turbid mediums with decreasing transparency from left to right. The standards 1, 2, 3, 4, 5 and 12 were directly used whereas the rest of the standards were diluted from maximum NTU standard solution. The values in Table 5.1 were also used to compare the FSL and spectrophotometric measurements.

Table 5.1: The turbidity values of formazin standard solutions (visually demonstrated in Figure 5.2a.)

Sample Name	NTU	Sample Name (Cont.)	NTU
Standard 1	0.43 ± 0.07	Standard 7	175.20 ± 1.10
Standard 2	3.53 ± 0.06	Standard 8	394.80 ± 1.79
Standard 3	12.88 ± 0.18	Standard 9	504.20 ± 1.48
Standard 4	27.72 ± 0.54	Standartd10	660.60 ± 2.07
Standard 5	56.66 ± 0.32	Standard 11	872.80 ± 4.82
Standard 6	100.80 ± 0.45	Standard 12	982.80 ± 4.32

5.3 Results

We first performed nephelometric SSL measurements on formazin standards using the smartphone turbidimeter. Here, five images were taken consecutively for each standard, and the average and standard deviation of the pixel information was extracted. The normalized Value spectrum was obtained for 12 standards after the spectrum for 0 NTU water was subtracted (Figure 5.2b). The 90° scattered light intensity increases with increasing number of suspended particles and there are two distinct peaks (~530nm and ~585nm) in the spectrum that are inherent to the smartphone flash LED source. In order to see Value as a function of turbidity and calibrate the smartphone turbidimeter, we used 585nm from the standard spectrum (Figure 5.2c). The trend is logarithmic, as it

tends to saturate with high NTU values. The inset graph shows the turbidity up to 40 NTU and its linear fit with R^2 value of 0.9928. The linear equation was later used to find the turbidity levels of unknown samples using SSL intensity. The limit of detection (LOD) was found to be 11.31 NTU, calculated as three standard deviations above the distilled water measurement. The sensitivity of the system, the slope of the inset graph, was found to be 0.0011 /NTU. Figure 5.2d shows the SSL spectral images with varying formazin concentrations. As can be seen, the color spectrum becomes more visible with higher NTU values due to increasing amount of light is being scattered.
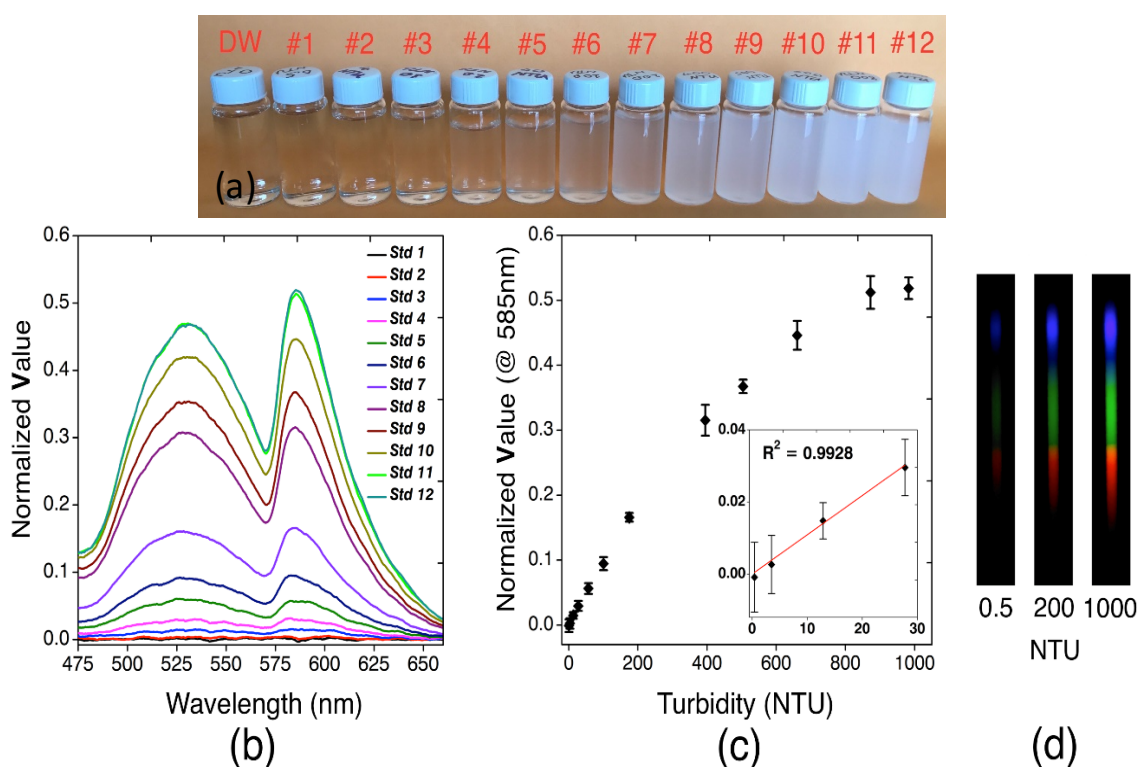
Figure 5.2 : a) The transparent nature of standard solutions decrease with increasing turbidity, b) Normalized SSL measurement spectrum for 12 standard solutions, c) The Values at 585nm are plotted against the turbidity of standards with an inset picture showing the 0-40 NTU region, d) The spectral images at 0.5, 200 and 1000 NTU levels.

The turbidity of standard solutions was also measured using both a commercial spectrophotometer (Hach DR 6000) and the smartphone turbidimeter. In Figure 5.3a, the absorbance of standard solutions shows gradually increasing behavior with increasing turbidity level. Moreover, the absorbance for a specific standard decreases with

increasing wavelength due to higher scattering at lower wavelengths. Considering the suspended particles are substantially larger than the wavelength of the light (i.e. Mie Scattering) as in the case of formazin standards, this behavior is expected owing to increasing surface area the light interacts with. In Figure 5.3b, absorbance at 585 nm versus turbidity for all standard solutions was plotted. The inset graph shows absorbance values linearly fitted between 0-40 NTU, with R^2 value of 0.9967. The LOD of forward scatter measurements of turbidity was found to be 5.58 NTU. The sensitivity of the system was found to be 0.0036 /NTU. Figure 5.3c shows the FSL spectral images with varying formazin concentrations. As can be seen, the color spectrum becomes less visible with higher NTU values due to increasing amount of light being blocked in the optical path. The spatial resolution is higher compared to SSL spectrum because of the plastic fiber size.
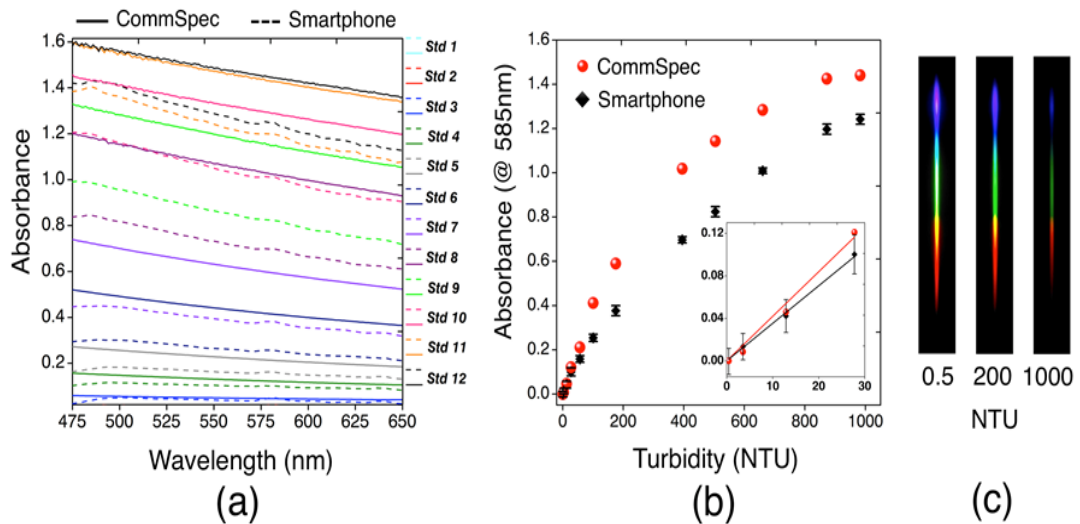
Figure 5.3 : a) FSL absorbance measurement spectrum for 12 standard solutions; b) The absorbance at 585nm for both Smartphone and Commercial Spectrometer systems are plotted against the turbidity of standards with an inset picture showing the 0-40 NTU region; c) The spectral images at 0.5, 200 and 1000 NTU levels showing decreasing color intensity as the FSL intensity decreases.

After calibrating the forward and side scattered light spectroscopic measurement modes, we tested the smartphone turbidimeter with water samples collected from natural resources near Izmir, Turkey. The environmental samples used in assessing the validity of the newly designed smartphone turbidimeter are selected from different matrices with

distinct characteristics. Figure 5.4a shows the map of Izmir region and the locations of the collected samples. Three samples were collected from mediums representing surface water resources where one sample represented subsurface water resources. The surface water samples were collected from the old and new channels of Gediz River, which is a main river in the region, and from the Bay of Izmir along the Bostanli shoreline in the Aegean Sea. Thus, the Bay of Izmir sample is essentially a saline water sample that shows the characteristics of seawater. The last sample was taken from a groundwater well situated in the Izmir Katip Celebi University campus. The well was drilled in the alluvial aquifer and is used to supply the domestic water needs of the campus. It must be noted that the samples characterize varying a wide turbidity range and this will help us demonstrate the capabilities of our newly designed smartphone turbidimeter. The NTU values obtained from the field are listed in Table 5.2. Furthermore, the particle size distribution (PSD) analysis was assessed using a Nano-Sizer (Malvern Instruments) and the mean and standard deviation of the size of the standard and sample solutions are extracted. It should be noted that our system was calibrated with standard solution of particle size 1990.0±613.0nm. Particle size larger than the wavelength of the light points to Mie scattering while the standard deviations potentially add more error to the smartphone based turbidimeter results. In addition to the measurements made by Hach nephelometric turbidimeter, turbidity values of the collected environmental samples were also measured by our newly designed smartphone turbidimeter. Figure 5.4b illustrate the sample turbidity values with both commercial systems (Hach spectrophotometric and turbidimeter) and smartphone FSL and SSL spectroscopic measurements. The measurements revealed a wide range of turbidity values representing the characteristics of the environmental medium the sample is taken from. The sample 3 from the Aegean Sea has the lowest turbidity values. For sea water samples taken from the shoreline, sampling period is critical with regards to turbidity. In other words, meteorological conditions and the associated sea conditions are critical. Windy seas create high waves that create turbid waters in sandy shorelines. The sample was taken on a fairly sunny and calm day with no major wave activity.
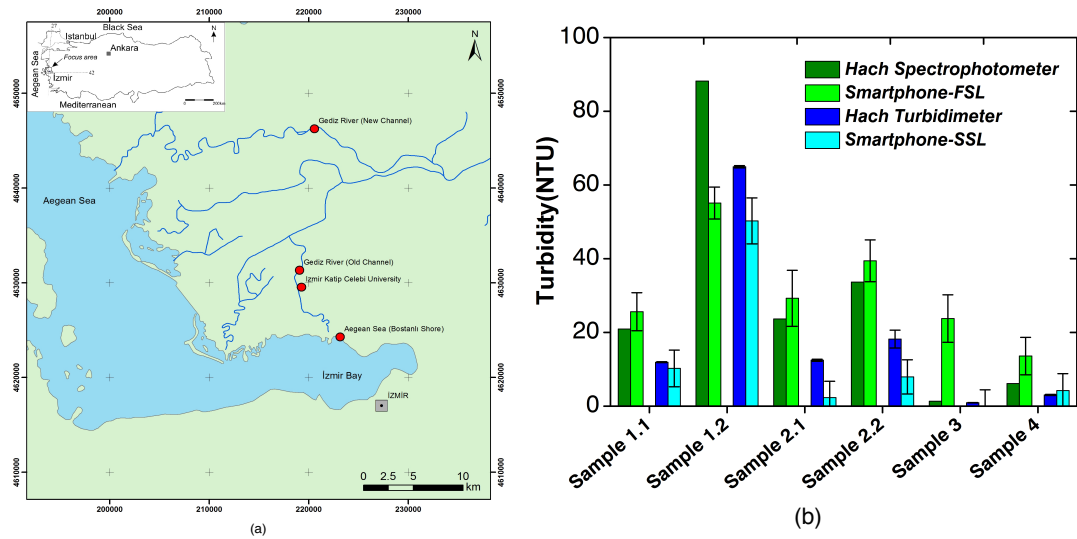
Figure 5.4 : The location map of the environmental samples used in checking the validity of the smartphone turbidimeter; b) The results of the turbidity measurements collected from 4 different field locations.

Thus, the sample had low turbidity values measured both with standard turbidimeter and the newly designed smartphone turbidimeter and also all results are given in Table 5.2.

Table 5.2: Sample measurements (NTU) measured with calibrated Hach nephelometric and smartphone turbidimeter, and respective particle size distributions

Sample	Sample Location	Hach	Smartphone SSL	PSD (nm)
Sample 1.1	Gediz River New Channel	11.92 ± 0.13	10.23 ± 4.98	615.1 ± 136.3
Sample 1.2	Gediz River New Channel	64.94 ± 0.32	50.26 ± 6.21	141.8 ± 16.6
Sample 2.1	Gediz River Old Channel	12.46 ± 0.30	2.33 ± 4.41	220.2 ± 29.5
Sample 2.2	Gediz River Old Channel	18.18 ± 2.43	7.94 ± 4.63	28.21 ± 4.6
Sample 3	Aegean Sea at Bostanli Shoreline	0.92 ± 0.05	0.05 ± 4.41	0.62 ± 0.06
Sample 4	Groundwater well at IKCU	3.04 ± 0.15	4.25 ± 4.56	531.2 ± 121.8

Similarly, sample 4 taken from groundwater also has a low turbidity value. This is an expected result since water in a sufficiently-developed groundwater well represents a sample coming from a filtered medium where turbidity causing particles are retained within the porous medium. This sample was taken from a well, which was under active operation for more than several years, and the extracted water is relatively clear and turbidity free. On the other hand, samples 1 and 2 are taken from a surface water body (i.e., Gediz River channel), which receives heavy domestic and industrial waste loads from its watershed. The old and new channels are the two drainage canals of the Gediz River, where the old channel is no longer carrying the active discharge of the river but still contains stagnant water inside. The new channel is the active canal carrying the Gediz River flow, and hence is prone to point and non-point discharges. The samples from these points were analyzed in two different ways: (i) first measurements (Samples 1.1. and 2.1) were made from the samples after settleable turbidity causing particles were allowed to settle made and (ii) a second set of measurements (Samples 1.2 and 2.2) were made immediately after the samples were taken. Thus, the second set measurement results were recorded to be less than the initial measurements made immediately. Here, the sample from the active channel that contained more turbidity causing particles in the river flow had about 5 fold difference, whereas the second sample from the old channel which did not receive any discharge from the main river was comparably clearer and less turbid. Hence, there was only about 1.5 folds difference between the immediate measurement and the time-delayed measurement.

Overall, the measurements with the newly designed Smartphone Turbidimeter were close to the values obtained from the industry standard turbidimeter (Table 5.2). In general, the results revealed that the smaller the natural turbidity of the sample, the poorer the readings made by our designed tool due to relatively large LOD. For instance, the results obtained from high turbid water samples 1.2 and 2.2 were closer to the values read by the Hach spectrometer measurements. On the other hand, the fairly clear low turbidity sample measurements were more distant to the values read by Hach spectrometer. Thus, it can be concluded that the newly designed tool performs more accurately at the moderate to high end of the turbidity spectrum. When the sample

65

turbidity decreases significantly, the results obtained from our tool starts to deviate from the values measured by industry standard devices owing to large noise level. Our proposed system's signal-to-noise ratio can further be improved using lenses to focus the collected light onto plastic fibers. Nevertheless, the tool is still very promising due to its flexibility, portability and overall cost.

5.4 Conclusion

In this study, we have designed and developed a portable, low-cost smartphone turbidimeter based on spectroscopic measurements of scattered light. The device is based on the principle of processing the color spectral images in RAW format to obtain spectrum data that was later related to turbidity. The smartphone turbidimeter was able to measure turbidity using forward scattered light and absorbance as well as normalized side scattered light. The performance of the proposed system was compared to commercial spectrophotometer and nephelometric turbidimeter. The sensing platform's limit of detection was found to be 5.58 NTU for SSL method while the dynamic range was 0-1000 NTU. The LOD values of FSL and SSL turbidity measurement methods were larger compared to commercial systems. The smartphone turbidimeter was also tested with real water samples collected from natural water resources and was found to perform more accurately at the moderate to high end of the turbidity spectrum. The results of this study indicate that the proposed spectroscopy based turbidimeter can provide a new line of technology that can open new horizons for eventually replacing benchtop spectrophotometers and hand-held turbidimeters for field-deployable water quality instrumentation. The LOD performance can be further improved by increasing signal-to-noise ratio via adjustments to the optical design. The practical use of this technology can be further improved by developing a smartphone application that is able to automatically process taken images. Furthermore, this technological development can lead to new lines of research for field measurement of additional water quality parameters.

6. MAIN CONCLUSION AND FUTURE WORK

This thesis describes development of 3D-printed plastic based low-cost sensing systems.

In the first part, health-environment relations, their interdependency and diseases arising from pollutions are discussed. The need of a reliable, low-cost and portable health and environment monitoring systems are emphasized. Here, the microfluidic devices and smartphone devices were offered as good candidates for these systems with the help of 3D printing production methods. The descriptions were supported with related literature information about 3D-printed microfluidic devices and 3D-printed smartphone based detection devices.

In the second part, theoretical information was given. Light-matter interaction and diffraction grating physics were discussed.

The third part presents a facile strategy for fabricating a microfluidic flow cytometer using two glass micropipettes of different sizes, and a corresponding 3D-printed millifluidic aligner. The 3D-printed aligner was precisely manufactured to allow easy alignment. DLP printing technology was chosen for the fabrication of the aligner to obtain good surface finish and high precision. The complete solid body was fabricated with chemically bonded consecutive layers, using DLP. FDM was rejected due to liquid leakage issues and flaws in the alignment process. During the DLP manufacturing process the aligner was printed with deviations of 5% and 1.5% for thin and thick capillaries, respectively. The wettability of the printed surface was tested through water contact angle and found to be 37.1° degree. The surface wettability of the device is important for microfluidic application to maintain the flow control. Throughout the entire fabrication, durable printing material was used to avoid degradation. The fabricated product is an ultra-low-cost, easy and rapidly-producible integrated system. In tests, the six-micron diameter polystyrene spheres were confined by sample and sheath flow. Side-scattered and forward-scattered optical signals were collected with fiber-coupled laser and photo detectors. The results were processed with MATLAB software. According to our tests, 170 polystyrene particles were counted per second. We observed

that some technical aspects of the aligner must be optimized before commercializing the aligner. These include the following: (1) Optimization of geometry to increase tunability range of pressure/focus ratios, (2) Usage of less complex test setup to lower noise, (3) More robust assembly of the capillary and plastic part to prevent liquid leakage, (4) Getting rid of the vibrations arising from blob dropping of fluidic channel, (5) More devices need to be tested with micro particles and cells to clarify the aligner's performance. The presented device offers a great alternative to conventional benchtop flow cytometers in terms of optofluidic configuration.

In the fourth part, a novel health-disrupting agent detection system was proposed, based on the colorimetric perception ability of smartphones. The best-known endocrine disrupting agent is Bisphenol A (BPA), used as a key monomer in the plastic industry. The low-cost and portability of our manufactured system, which uses the FDM printing method, makes it ideal for developing countries. We conducted an experimental study based on color change caused by the formation of the quinone type complex. Experiments were conducted in alkaline aqueous environments, using samples obtained from two different sources – distilled and commercial drinking water. The proposed smartphone-based spectrometer succeeded in detecting the lowest limit of 0.2 mg/L. In the manufacturing method of the spectrometer's plastic components, price was the sole factor, since surface properties and precision were not a priority in this application. Thus, an extrusion-based manufacturing method was chosen to form a model using ABS polymer. Happily, we achieved a manufactured final product with a total cost of under 5$. Furthermore, our product perfectly blocks light, isolating the spectrometer system from the external environment via black polymer. We note that the spectrometer's components should be firmly fixed to use it as a handheld spectrometer. In addition, the shining metal that reflects the light may corrode; therefore, it should be replaced or polished over time.

In fifth part, the application of a low-cost smartphone turbidimeter system for water samples collected from natural resources were demonstrated for the benefit of public health. The proposed system depends on the spectroscopic measurements of both

forward and side scattered light on sample water. To implement this system, a custom-designed cradle was fabricated using the PDM 3D printing technique, and plastic optical fibers were used to couple light from the smartphone's inbuilt flashlight and transmit the collected scattered light into the camera sensor. The performance parameters of the smartphone turbidimeter were investigated and compared to commercial systems. The lowest limit of detection was 5.58 NTU for side-scattered light. The system's working principle is based on Mie scattering, where measurement instabilities should be reduced when light has high wavelength. The corresponding instabilities were reported with respect to standard deviation. The deviation problem requires removal of large suspended particles; therefore, the sample preparation process should include filtering. Finally, I note that smartphone cradle, sample holder and fiber cables should be fixed for continuous measurement. The results obtained from the proposed low-cost scattered-light-based spectroscopic turbidimeter have crucial significance for water science and technology, and public health.

REFERENCES

[1] **Callahan, D.,** (1973). *The WHO definition of'health'.* Hastings Center Studies: p. 77-87.

[2] **Arbes, S.J., P.J. Gergen, L. Elliott, and D.C. Zeldin,** (2005). *Prevalences of positive skin test responses to 10 common allergens in the US population: results from the third National Health and Nutrition Examination Survey.* Journal of Allergy and Clinical Immunology, 116(2): p. 377-383.

[3] **Patnaik, P.,** (2007), *A comprehensive guide to the hazardous properties of chemical substances.* John Wiley & Sons.

[4] **Forouzanfar, M.H., L. Alexander, H.R. Anderson, V.F. Bachman, S. Biryukov, M. Brauer, R. Burnett, D. Casey, M.M. Coates, and A. Cohen,** (2015). *Global, regional, and national comparative risk assessment of 79 behavioural, environmental and occupational, and metabolic risks or clusters of risks in 188 countries, 1990–2013: a systematic analysis for the Global Burden of Disease Study 2013.* The Lancet, 386(10010): p. 2287-2323.

[5] **Israel, B.A., E.A. Parker, Z. Rowe, A. Salvatore, M. Minkler, J. López, A. Butz, A. Mosley, L. Coates, and G. Lambert,** (2005). *Community-based participatory research: lessons learned from the Centers for Children's Environmental Health and Disease Prevention Research.* Environmental health perspectives, 113(10): p. 1463.

[6] **Kampa, M. and E. Castanas,** (2008). *Human health effects of air pollution.* Environmental pollution, 151(2): p. 362-367.

[7] **Landrigan, P.J., C.B. Schechter, J.M. Lipton, M.C. Fahs, and J. Schwartz,** (2002). *Environmental pollutants and disease in American children: estimates of morbidity, mortality, and costs for lead poisoning, asthma, cancer, and developmental disabilities.* Environmental health perspectives, 110(7): p. 721.

[8] **Framework, I.C.C.M.,** (2011). *checklist and indicators for monitoring progress in the development of IHR core capacities in States Parties.* World Health Organization, http://www/. who. int/ihr/IHR_Monitoring_Framework_Checklist_and_Indicators. pdf.

[9] **Aitken, R. and K. Leithwood,** (1995), *Making Schools Smarter: A system for monitoring school and district progress.* Thousand Oaks, CA: Corwin Press.

[10] **Magnusson, R.,** (2017). *Advancing the right to health: the vital role of law.*

[11] **Beck, I.-C., R. Bruhn, J. Gandrass, and W. Ruck,** (2005). *Liquid chromatography–tandem mass spectrometry analysis of estrogenic compounds in coastal surface water of the Baltic Sea.* Journal of Chromatography A, 1090(1): p. 98-106.

[12] **Rezaee, M., Y. Yamini, S. Shariati, A. Esrafili, and M. Shamsipur,** (2009). *Dispersive liquid–liquid microextraction combined with high-performance liquid chromatography-UV detection as a very simple, rapid and sensitive method for the determination of bisphenol A in water samples.* Journal of Chromatography A, 1216(9): p. 1511-1514.

[13] **Meng, J., C. Shi, B. Wei, W. Yu, C. Deng, and X. Zhang,** (2011). *Preparation of Fe 3 O 4@ C@ PANI magnetic microspheres for the extraction and analysis of phenolic compounds in water samples by gas chromatography–mass spectrometry.* Journal of Chromatography A, 1218(20): p. 2841-2847.

[14] **Mei, Z., H. Chu, W. Chen, F. Xue, J. Liu, H. Xu, R. Zhang, and L. Zheng,** (2013). *Ultrasensitive one-step rapid visual detection of bisphenol A in water samples by label-free aptasensor.* Biosensors and Bioelectronics, 39(1): p. 26-30.

[15] **Jin, X., G. Jiang, G. Huang, J. Liu, and Q. Zhou,** (2004). *Determination of 4-tert-octylphenol, 4-nonylphenol and bisphenol A in surface waters from the Haihe River in Tianjin by gas chromatography–mass spectrometry with selected ion monitoring.* Chemosphere, 56(11): p. 1113-1119.

[16] **Del Olmo, M., A. Gonzalez-Casado, N. Navas, and J. Vilchez,** (1997). *Determination of bisphenol A (BPA) in water by gas chromatography-mass spectrometry.* Analytica Chimica Acta, 346(1): p. 87-92.

[17] **Gawad, S., L. Schild, and P. Renaud,** (2001). *Micromachined impedance spectroscopy flow cytometer for cell analysis and particle sizing.* Lab on a Chip, 1(1): p. 76-82.

[18] **Amann, R.I., B.J. Binder, R.J. Olson, S.W. Chisholm, R. Devereux, and D.A. Stahl,** (1990). *Combination of 16S rRNA-targeted oligonucleotide probes with flow cytometry for analyzing mixed microbial populations.* Applied and environmental microbiology, 56(6): p. 1919-1925.

[19] **Whitesides, G.M.,** (2006). *The origins and the future of microfluidics.* Nature, 442(7101): p. 368.

[20] **Yeo, L.Y., H.C. Chang, P.P. Chan, and J.R. Friend,** (2011). *Microfluidic devices for bioapplications.* small, 7(1): p. 12-48.

[21] **Boone, T.D., Z.H. Fan, H.H. Hooper, A.J. Ricco, H. Tan, and S.J. Williams,** (2002), *Peer reviewed: plastic advances microfluidic devices.* ACS Publications.

[22] **Silverio, V. and S.C. de Freitas,** (2018),*Microfabrication Techniques for Microfluidic Devices*, in *Complex Fluid-Flows in Microfluidics*. Springer. p. 25-51.

[23] **Petti, C.A., C.R. Polage, T.C. Quinn, A.R. Ronald, and M.A. Sande,** (2006). *Laboratory medicine in Africa: a barrier to effective health care.* Clinical Infectious Diseases, 42(3): p. 377-382.

[24] **Marle, L. and G.M. Greenway,** (2005). *Microfluidic devices for environmental monitoring.* TrAC Trends in Analytical Chemistry, 24(9): p. 795-802.

[25] **Becker, H. and C. Gärtner,** (2000). *Polymer microfabrication methods for microfluidic analytical applications.* Electrophoresis, 21(1): p. 12-26.

[26] **Lane, N.D., E. Miluzzo, H. Lu, D. Peebles, T. Choudhury, and A.T. Campbell,** (2010). *A survey of mobile phone sensing.* IEEE Communications magazine, 48(9).

[27] **Martinez, A.W., S.T. Phillips, E. Carrilho, S.W. Thomas III, H. Sindi, and G.M. Whitesides,** (2008). *Simple telemedicine for developing regions: camera phones and paper-based microfluidic devices for real-time, off-site diagnosis.* Analytical chemistry, 80(10): p. 3699-3707.

[28] Lee, W.G., Y.-G. Kim, B.G. Chung, U. Demirci, and A. Khademhosseini, (2010). *Nano/Microfluidics for diagnosis of infectious diseases in developing countries.* Advanced drug delivery reviews, 62(4-5): p. 449-457.

[29] Zhu, H., S. Mavandadi, A.F. Coskun, O. Yaglidere, and A. Ozcan, (2011). *Optofluidic fluorescent imaging cytometry on a cell phone.* Analytical chemistry, 83(17): p. 6641-6647.

[30] Mueller, B., (2012). *Additive manufacturing technologies–Rapid prototyping to direct digital manufacturing.* Assembly Automation, 32(2).

[31] Gowers, S.A., V.F. Curto, C.A. Seneci, C. Wang, S. Anastasova, P. Vadgama, G.-Z. Yang, and M.G. Boutelle, (2015). *3D printed microfluidic device with integrated biosensors for online analysis of subcutaneous human microdialysate.* Analytical chemistry, 87(15): p. 7763-7770.

[32] Petrick, I.J. and T.W. Simpson, (2013). *3D printing disrupts manufacturing: how economies of one create new rules of competition.* Research-Technology Management, 56(6): p. 12-16.

[33] Crump, S.S., (1992), *Apparatus and method for creating three-dimensional objects.* Google Patents.

[34] Pham, D.T. and R.S. Gault, (1998). *A comparison of rapid prototyping technologies.* International Journal of machine tools and manufacture, 38(10): p. 1257-1287.

[35] Ziemian, C. and P. Crawn III, (2001). *Computer aided decision support for fused deposition modeling.* Rapid Prototyping Journal, 7(3): p. 138-147.

[36] Sood, A.K., R. Ohdar, and S.S. Mahapatra, (2009). *Improving dimensional accuracy of fused deposition modelling processed part using grey Taguchi method.* Materials & Design, 30(10): p. 4243-4252.

[37] Zhong, W., F. Li, Z. Zhang, L. Song, and Z. Li, (2001). *Short fiber reinforced composites for fused deposition modeling.* Materials Science and Engineering: A, 301(2): p. 125-130.

[38] Wu, G., N.A. Langrana, R. Sadanji, and S. Danforth, (2002). *Solid freeform fabrication of metal components using fused deposition of metals.* Materials & design, 23(1): p. 97-105.

[39] Jafari, M., W. Han, F. Mohammadi, A. Safari, S. Danforth, and N. Langrana, (2000). *A novel system for fused deposition of advanced multiple ceramics.* Rapid Prototyping Journal, 6(3): p. 161-175.

[40] Zein, I., D.W. Hutmacher, K.C. Tan, and S.H. Teoh, (2002). *Fused deposition modeling of novel scaffold architectures for tissue engineering applications.* Biomaterials, 23(4): p. 1169-1185.

[41] Shao, H., X. Yang, Y. He, J. Fu, L. Liu, L. Ma, L. Zhang, G. Yang, C. Gao, and Z. Gou, (2015). *Bioactive glass-reinforced bioceramic ink writing scaffolds: sintering, microstructure and mechanical behavior.* Biofabrication, 7(3): p. 035010.

[42] Bogue, R., (2013). *3D printing: the dawn of a new era in manufacturing?* Assembly Automation, 33(4): p. 307-311.

[43] **Lu, Y., G. Mapili, G. Suhali, S. Chen, and K. Roy,** (2006). *A digital micro-mirror device-based system for the microfabrication of complex, spatially patterned tissue engineering scaffolds.* Journal of Biomedical Materials Research Part A, 77(2): p. 396-405.

[44] **Choi, J.-W., R. Wicker, S.-H. Lee, K.-H. Choi, C.-S. Ha, and I. Chung,** (2009). *Fabrication of 3D biocompatible/biodegradable micro-scaffolds using dynamic mask projection microstereolithography.* Journal of Materials Processing Technology, 209(15): p. 5494-5503.

[45] **Han, L.-H., G. Mapili, S. Chen, and K. Roy,** (2008). *Projection microfabrication of three-dimensional scaffolds for tissue engineering.* Journal of Manufacturing Science and Engineering, 130(2): p. 021005.

[46] **Chua, C.-K., W.-Y. Yeong, and K.-F. Leong.** (2005)*Rapid prototyping in tissue engineering: a state-of-the-art report.* in *Proc. 2nd Int. Conf. on Advanced Research in Virtual and Rapid Prototyping.*

[47] **Khoo, Z.X., J.E.M. Teoh, Y. Liu, C.K. Chua, S. Yang, J. An, K.F. Leong, and W.Y. Yeong,** (2015). *3D printing of smart materials: A review on recent progresses in 4D printing.* Virtual and Physical Prototyping, 10(3): p. 103-122.

[48] **Vaezi, M. and S. Yang,** (2015). *A novel bioactive PEEK/HA composite with controlled 3D interconnected HA network.* International Journal of Bioprinting, 1(1).

[49] **Yeong, W.-Y., C.-K. Chua, K.-F. Leong, M. Chandrasekaran, and M.-W. Lee,** (2005). *Development of scaffolds for tissue engineering using a 3D inkjet model maker.* Virtual modelling and rapid manufacturing-advanced research in virtual and rapid prototyping: p. 115-118.

[50] **Waldbaur, A., H. Rapp, K. Laenge, and B.E. Rapp,** (2011). *Let there be chip—towards rapid prototyping of microfluidic devices: one-step manufacturing processes.* Analytical Methods, 3(12): p. 2681-2716.

[51] **Ho, C.M.B., S.H. Ng, K.H.H. Li, and Y.-J. Yoon,** (2015). *3D printed microfluidics for biological applications.* Lab on a Chip, 15(18): p. 3627-3637.

[52] **McDonald, J.C., M.L. Chabinyc, S.J. Metallo, J.R. Anderson, A.D. Stroock, and G.M. Whitesides,** (2002). *Prototyping of microfluidic devices in poly (dimethylsiloxane) using solid-object printing.* Analytical chemistry, 74(7): p. 1537-1545.

[53] **Yenilmez, B., S. Knowlton, C.H. Yu, M.M. Heeney, and S. Tasoglu,** (2016). *Label-free sickle cell disease diagnosis using a low-cost, handheld platform.* Advanced Materials Technologies, 1(5).

[54] **Lee, W., D. Kwon, W. Choi, G.Y. Jung, A.K. Au, A. Folch, and S. Jeon,** (2015). *3D-printed microfluidic device for the detection of pathogenic bacteria using size-based separation in helical channel with trapezoid cross-section.* Scientific reports, 5: p. 7717.

[55] **Chudobova, D., K. Cihalova, S. Skalickova, J. Zitka, M.A.M. Rodrigo, V. Milosavljevic, D. Hynek, P. Kopel, R. Vesely, and V. Adam,** (2015). *3D-printed chip for detection of methicillin-resistant Staphylococcus aureus labeled with gold nanoparticles.* Electrophoresis, 36(3): p. 457-466.

[56] Takenaga, S., B. Schneider, E. Erbay, M. Biselli, T. Schnitzler, M.J. Schöning, and T. Wagner, (2015). *Fabrication of biocompatible lab-on-chip devices for biomedical applications by means of a 3D-printing process.* physica status solidi (a), 212(6): p. 1347-1352.

[57] Anderson, K.B., S.Y. Lockwood, R.S. Martin, and D.M. Spence, (2013). *A 3D printed fluidic device that enables integrated features.* Analytical chemistry, 85(12): p. 5622-5626.

[58] Erkal, J.L., A. Selimovic, B.C. Gross, S.Y. Lockwood, E.L. Walton, S. McNamara, R.S. Martin, and D.M. Spence, (2014). *3D printed microfluidic devices with integrated versatile and reusable electrodes.* Lab on a Chip, 14(12): p. 2023-2032.

[59] Vlachova, J., K. Tmejova, P. Kopel, M. Korabik, J. Zitka, D. Hynek, J. Kynicky, V. Adam, and R. Kizek, (2015). *A 3D microfluidic chip for electrochemical detection of hydrolysed nucleic bases by a modified glassy carbon electrode.* Sensors, 15(2): p. 2438-2452.

[60] Gao, Q., Y. He, J.-z. Fu, A. Liu, and L. Ma, (2015). *Coaxial nozzle-assisted 3D bioprinting with built-in microchannels for nutrients delivery.* Biomaterials, 61: p. 203-215.

[61] Bhargava, K.C., B. Thompson, and N. Malmstadt, (2014). *Discrete elements for 3D microfluidics.* Proceedings of the National Academy of Sciences, 111(42): p. 15013-15018.

[62] Jue, E., N.G. Schoepp, D. Witters, and R.F. Ismagilov, (2016). *Evaluating 3D printing to solve the sample-to-device interface for LRS and POC diagnostics: example of an interlock meter-mix device for metering and lysing clinical urine samples.* Lab on a Chip, 16(10): p. 1852-1860.

[63] Lockwood, S.Y., J.E. Meisel, F.J. Monsma Jr, and D.M. Spence, (2016). *A diffusion-based and dynamic 3D-printed device that enables parallel in vitro pharmacokinetic profiling of molecules.* Analytical chemistry, 88(3): p. 1864-1870.

[64] Erickson, D., D. O'Dell, L. Jiang, V. Oncescu, A. Gumus, S. Lee, M. Mancuso, and S. Mehta, (2014). *Smartphone technology can be transformative to the deployment of lab-on-chip diagnostics.* Lab on a Chip, 14(17): p. 3159-3164.

[65] Xu, X., A. Akay, H. Wei, S. Wang, B. Pingguan-Murphy, B.-E. Erlandsson, X. Li, W. Lee, J. Hu, and L. Wang, (2015). *Advances in smartphone-based point-of-care diagnostics.* Proceedings of the IEEE, 103(2): p. 236-247.

[66] Martinez, A.W., S.T. Phillips, E. Carrilho, S.W. Thomas, H. Sindi, and G.M. Whitesides, (2008). *Simple Telemedicine for Developing Regions: Camera Phones and Paper-Based Microfluidic Devices for Real-Time, Off-Site Diagnosis.* Analytical Chemistry, 80(10): p. 3699-3707.

[67] Bellina, L. and E. Missoni, (2009). *Mobile cell-phones (M-phones) in telemicroscopy: increasing connectivity of isolated laboratories.* Diagnostic Pathology, 4(1): p. 19.

[68] **Roda, A., M.M. Calabretta, D. Calabria, C. Caliceti, L. Cevenini, A. Lopreside, and M. Zangheri,** (2017),*Smartphone-Based Biosensors for Bioanalytics: A Critical Review*, in *Comprehensive Analytical Chemistry*. Elsevier. p. 237-286.

[69] **Delaney, J.L., C.F. Hogan, J. Tian, and W. Shen,** (2011). *Electrogenerated chemiluminescence detection in paper-based microfluidic sensors.* Analytical chemistry, 83(4): p. 1300-1306.

[70] **Roda, A., E. Michelini, M. Zangheri, M. Di Fusco, D. Calabria, and P. Simoni,** (2016). *Smartphone-based biosensors: A critical review and perspectives.* TrAC Trends in Analytical Chemistry, 79: p. 317-325.

[71] **McCracken, K.E. and J.-Y. Yoon,** (2016). *Recent approaches for optical smartphone sensing in resource-limited settings: a brief review.* Analytical Methods, 8(36): p. 6591-6601.

[72] **Zhang, D. and Q. Liu,** (2016). *Biosensors and bioelectronics on smartphone for portable biochemical detection.* Biosensors and Bioelectronics, 75: p. 273-284.

[73] **Scheeline, A.,** (2016). *Cell phone spectrometry: Science in your pocket?* TrAC Trends in Analytical Chemistry, 85: p. 20-25.

[74] **Shen, L., J.A. Hagen, and I. Papautsky,** (2012). *Point-of-care colorimetric detection with a smartphone.* Lab on a Chip, 12(21): p. 4240-4243.

[75] **Breslauer, D.N., R.N. Maamari, N.A. Switz, W.A. Lam, and D.A. Fletcher,** (2009). *Mobile phone based clinical microscopy for global health applications.* PloS one, 4(7): p. e6320.

[76] **Tseng, D., O. Mudanyali, C. Oztoprak, S.O. Isikman, I. Sencan, O. Yaglidere, and A. Ozcan,** (2010). *Lensfree microscopy on a cellphone.* Lab on a Chip, 10(14): p. 1787-1792.

[77] **Zhu, H., O. Yaglidere, T.-W. Su, D. Tseng, and A. Ozcan,** (2011). *Cost-effective and compact wide-field fluorescent imaging on a cell-phone.* Lab on a Chip, 11(2): p. 315-322.

[78] **Navruz, I., A.F. Coskun, J. Wong, S. Mohammad, D. Tseng, R. Nagi, S. Phillips, and A. Ozcan,** (2013). *Smart-phone based computational microscopy using multi-frame contact imaging on a fiber-optic array.* Lab on a Chip, 13(20): p. 4015-4023.

[79] **Bishara, W., U. Sikora, O. Mudanyali, T.-W. Su, O. Yaglidere, S. Luckhart, and A. Ozcan,** (2011). *Holographic pixel super-resolution in portable lensless on-chip microscopy using a fiber-optic array.* Lab on a Chip, 11(7): p. 1276-1279.

[80] **Mudanyali, O., S. Dimitrov, U. Sikora, S. Padmanabhan, I. Navruz, and A. Ozcan,** (2012). *Integrated rapid-diagnostic-test reader platform on a cellphone.* Lab on a Chip, 12(15): p. 2678-2686.

[81] **Kerker, M.,** (1971). *The Scattering of Light and Other Electromagnetic Radiation (Academic, New York, 1969).* Google Scholar: p. 414.

[82] **Halliday, D., R. Resnick, and J. Walker,** (2010), *Fundamentals of Physics, Chapters 33-37.* John Wiley & Sons.

[83] **Hahn, D.W.,** (2009). *Light scattering theory.* Department of Mechanical and Aerospace Engineering, University of Florida.

[84] Wu, L., X. Wang, J. Zhang, T. Luan, E. Bouveret, and X. Yan, (2017). *Flow Cytometric Single-Cell Analysis for Quantitative in Vivo Detection of Protein–Protein Interactions via Relative Reporter Protein Expression Measurement.* Analytical Chemistry, 89(5): p. 2782-2789.

[85] Lehmann, A.K., S. Sornes, and A. Halstensen, (2000). *Phagocytosis: measurement by flow cytometry.* J Immunol Methods, 243(1-2): p. 229-42.

[86] Roederer, M., J.M. Brenchley, M.R. Betts, and S.C. De Rosa, (2004). *Flow cytometric analysis of vaccine responses: how many colors are enough?* Clinical Immunology, 110(3): p. 199-205.

[87] Weir, E.G. and M.J. Borowitz, (2001). *Flow cytometry in the diagnosis of acute leukemia.* Semin Hematol, 38(2): p. 124-38.

[88] Peters, J.M. and M.Q. Ansari, (2011). *Multiparameter flow cytometry in the diagnosis and management of acute leukemia.* Arch Pathol Lab Med, 135(1): p. 44-54.

[89] Theunissen, P., E. Mejstrikova, L. Sedek, A.J. van der Sluijs-Gelling, G. Gaipa, M. Bartels, E. Sobral da Costa, M. Kotrová, M. Novakova, E. Sonneveld, C. Buracchi, P. Bonaccorso, E. Oliveira, J.G. te Marvelde, T. Szczepanski, L. Lhermitte, O. Hrusak, Q. Lecrevisse, G.E. Grigore, E. Froňková, J. Trka, M. Brüggemann, A. Orfao, J.J.M. van Dongen, and V.H.J. van der Velden, (2017). *Standardized flow cytometry for highly sensitive MRD measurements in B-cell acute lymphoblastic leukemia.* Blood, 129(3): p. 347-357.

[90] Fromm, J.R., A. Thomas, and B.L. Wood, (2009). *Flow Cytometry Can Diagnose Classical Hodgkin Lymphoma in Lymph Nodes With High Sensitivity and Specificity.* American Journal of Clinical Pathology, 131(3): p. 322-332.

[91] Cozzolino, I., M. Rocco, G. Villani, and M. Picardi, (2016). *Lymph Node Fine-Needle Cytology of Non-Hodgkin Lymphoma: Diagnosis and Classification by Flow Cytometry.* Acta Cytologica, 60(4): p. 302-314.

[92] Clift, I.C., (2015). *Diagnostic Flow Cytometry and the AIDS Pandemic.* Laboratory Medicine, 46(3): p. e59-e64.

[93] Waldrop, S.L., C.J. Pitcher, D.M. Peterson, V.C. Maino, and L.J. Picker, (1997). *Determination of antigen-specific memory/effector CD4+ T cell frequencies by flow cytometry: evidence for a novel, antigen-specific homeostatic mechanism in HIV-associated immunodeficiency.* J Clin Invest, 99(7): p. 1739-50.

[94] Eluru, G., L.A.N. Julius, and S.S. Gorthi, (2016). *Single-layer microfluidic device to realize hydrodynamic 3D flow focusing.* Lab on a Chip, 16(21): p. 4133-4141.

[95] Testa, G., G. Persichetti, and R. Bernini, (2015). *Micro flow cytometer with self-aligned 3D hydrodynamic focusing.* Biomedical Optics Express, 6(1): p. 54-62.

[96] Paie, P., F. Bragheri, R.M. Vazquez, and R. Osellame, (2014). *Straightforward 3D hydrodynamic focusing in femtosecond laser fabricated microfluidic channels.* Lab on a Chip, 14(11): p. 1826-1833.

[97] Tripathi, S., A. Kumar, Y.V. Bala Varun Kumar, and A. Agrawal, (2016). *Three-dimensional hydrodynamic flow focusing of dye, particles and cells in a*

microfluidic device by employing two bends of opposite curvature. Microfluidics and Nanofluidics, 20(2): p. 34.

[98] **Chu, H., I. Doh, and Y.-H. Cho,** (2009). *A three-dimensional (3D) particle focusing channel using the positive dielectrophoresis (pDEP) guided by a dielectric structure between two planar electrodes.* Lab on a Chip, 9(5): p. 686-691.

[99] **Yan, S., J. Zhang, M. Li, G. Alici, H. Du, R. Sluyter, and W. Li,** (2014). *On-chip high-throughput manipulation of particles in a dielectrophoresis-active hydrophoretic focuser.* Scientific Reports, 4: p. 5060.

[100] **Shi, J., S. Yazdi, S.C. Lin, X. Ding, I.K. Chiang, K. Sharp, and T.J. Huang,** (2011). *Three-dimensional continuous particle focusing in a microfluidic channel via standing surface acoustic waves (SSAW).* Lab Chip, 11(14): p. 2319-24.

[101] **Yang, A.H. and H.T. Soh,** (2012). *Acoustophoretic sorting of viable mammalian cells in a microfluidic device.* Anal Chem, 84(24): p. 10756-62.

[102] **Chen, Y., A.A. Nawaz, Y. Zhao, P.-H. Huang, J.P. McCoy, S.J. Levine, L. Wang, and T.J. Huang,** (2014). *Standing surface acoustic wave (SSAW)-based microfluidic cytometer.* Lab on a Chip, 14(5): p. 916-923.

[103] **Augustsson, P., J.T. Karlsen, H.-W. Su, H. Bruus, and J. Voldman,** (2016). *Iso-acoustic focusing of cells for size-insensitive acousto-mechanical phenotyping.* Nature Communications, 7: p. 11556.

[104] **Jia, Y., Y. Ren, and H. Jiang,** (2015). *Continuous-flow focusing of microparticles using induced-charge electroosmosis in a microfluidic device with 3D AgPDMS electrodes.* RSC Advances, 5(82): p. 66602-66610.

[105] **Liu, Z., A.J.H. Frijns, M.F.M. Speetjens, and A.A. van Steenhoven,** (2015). *Particle focusing by AC electroosmosis with additional axial flow.* Microfluidics and Nanofluidics, 18(5): p. 1115-1129.

[106] **Ren, Y., J. Liu, W. Liu, Q. Lang, Y. Tao, Q. Hu, L. Hou, and H. Jiang,** (2016). *Scaled particle focusing in a microfluidic device with asymmetric electrodes utilizing induced-charge electroosmosis.* Lab on a Chip, 16(15): p. 2803-2812.

[107] **Jingjing, Z. and Y. Zheng,** (2015). *Microfluidic hydrodynamic focusing for high-throughput applications.* Journal of Micromechanics and Microengineering, 25(12): p. 125006.

[108] **Nawaz, A.A., X. Zhang, X. Mao, J. Rufo, S.C. Lin, F. Guo, Y. Zhao, M. Lapsley, P. Li, J.P. McCoy, S.J. Levine, and T.J. Huang,** (2014). *Sub-micrometer-precision, three-dimensional (3D) hydrodynamic focusing via "microfluidic drifting".* Lab Chip, 14(2): p. 415-23.

[109] **Sundararajan, N., M.S. Pio, L.P. Lee, and A.A. Berlin,** (2004). *Three-dimensional hydrodynamic focusing in polydimethylsiloxane (PDMS) microchannels.* Journal of Microelectromechanical Systems, 13(4): p. 559-567.

[110] **Gottmann, J., M. Hermans, N. Repiev, and J. Ortmann,** (2017). *Selective Laser-Induced Etching of 3D Precision Quartz Glass Components for Microfluidic Applications—Up-Scaling of Complexity and Speed.* Micromachines, 8(4): p. 110.

[111] Utada, A.S., E. Lorenceau, D.R. Link, P.D. Kaplan, H.A. Stone, and D.A. Weitz, (2005). *Monodisperse double emulsions generated from a microcapillary device.* Science, 308(5721): p. 537-41.

[112] Kim, S.H., J.W. Kim, J.C. Cho, and D.A. Weitz, (2011). *Double-emulsion drops with ultra-thin shells for capsule templates.* Lab Chip, 11(18): p. 3162-6.

[113] Sen, M. and A. Demirci, (2016). *pH-Dependent ionic-current-rectification in nanopipettes modified with glutaraldehyde cross-linked protein membranes.* RSC Advances, 6(89): p. 86334-86339.

[114] Sen, M., K. Ino, H. Shiku, and T. Matsue, (2012). *A new electrochemical assay method for gene expression using HeLa cells with a secreted alkaline phosphatase (SEAP) reporter system.* Biotechnol Bioeng, 109(8): p. 2163-7.

[115] Sen, M., Y. Takahashi, Y. Matsumae, Y. Horiguchi, A. Kumatani, K. Ino, H. Shiku, and T. Matsue, (2015). *Improving the electrochemical imaging sensitivity of scanning electrochemical microscopy-scanning ion conductance microscopy by using electrochemical Pt deposition.* Anal Chem, 87(6): p. 3484-9.

[116] Simonnet, C. and A. Groisman, (2006). *High-Throughput and High-Resolution Flow Cytometry in Molded Microfluidic Devices.* Analytical Chemistry, 78(16): p. 5653-5663.

[117] Chapin, R.E., J. Adams, K. Boekelheide, L.E. Gray, S.W. Hayward, P.S. Lees, B.S. McIntyre, K.M. Portier, T.M. Schnorr, and S.G. Selevan, (2008). *NTP-CERHR expert panel report on the reproductive and developmental toxicity of bisphenol A.* Birth Defects Research Part B: Developmental and Reproductive Toxicology, 83(3): p. 157-395.

[118] Vandenberg, L.N., M.V. Maffini, C. Sonnenschein, B.S. Rubin, and A.M. Soto, (2009). *Bisphenol-A and the great divide: a review of controversies in the field of endocrine disruption.* Endocrine Reviews, 30(1): p. 75-95.

[119] Schug, T.T., A. Janesick, B. Blumberg, and J.J. Heindel, (2011). *Endocrine disrupting chemicals and disease susceptibility.* The Journal of Steroid Biochemistry and Molecular Biology, 127(3): p. 204-215.

[120] Krishnan, A.V., P. Stathis, S.F. Permuth, L. Tokes, and D. Feldman, (1993). *Bisphenol-A: an estrogenic substance is released from polycarbonate flasks during autoclaving.* Endocrinology, 132(6): p. 2279-2286.

[121] Vom Saal, F.S. and C. Hughes, (2005). *An extensive new literature concerning low-dose effects of bisphenol A shows the need for a new risk assessment.* Environmental Health Perspectives: p. 926-933.

[122] Rubin, B.S., (2011). *Bisphenol A: an endocrine disruptor with widespread exposure and multiple effects.* The Journal of Steroid Biochemistry and Molecular Biology, 127(1): p. 27-34.

[123] Cabaton, N.J., P.R. Wadia, B.S. Rubin, D. Zalko, C.M. Schaeberle, M.H. Askenase, J.L. Gadbois, A.P. Tharp, G.S. Whitt, and C. Sonnenschein, (2011). *Perinatal exposure to environmentally relevant levels of bisphenol A decreases fertility and fecundity in CD-1 mice.* Environmental Health Perspectives, 119(4): p. 547.

[124] **Howdeshell, K.L., P.H. Peterman, B.M. Judy, J.A. Taylor, C.E. Orazio, R.L. Ruhlen, F.S. Vom Saal, and W.V. Welshons,** (2003). *Bisphenol A is released from used polycarbonate animal cages into water at room temperature.* Environmental Health Perspectives, 111(9): p. 1180.

[125] **Dark, W., E. Conrad, and L. Crossman,** (1974). *Liquid chromatographic analysis of epoxy resins.* Journal of Chromatography A, 91: p. 247-260.

[126] **Cao, X.-L. and J. Corriveau,** (2008). *Survey of bisphenol A in bottled water products in Canada.* Food Additives and Contaminants, 1(2): p. 161-164.

[127] **Cao, X.-L. and J. Corriveau,** (2008). *Migration of bisphenol A from polycarbonate baby and water bottles into water under severe conditions.* Journal of Agricultural and Food Chemistry, 56(15): p. 6378-6381.

[128] **Li, X., G.-G. Ying, J.-L. Zhao, Z.-F. Chen, H.-J. Lai, and H.-C. Su,** (2013). *4-Nonylphenol, bisphenol-A and triclosan levels in human urine of children and students in China, and the effects of drinking these bottled materials on the levels.* Environment International, 52: p. 81-86.

[129] **Vandenberg, L.N., R. Hauser, M. Marcus, N. Olea, and W.V. Welshons,** (2007). *Human exposure to bisphenol A (BPA).* Reproductive Toxicology, 24(2): p. 139-177.

[130] **Zhao, M.-P., Y.-Z. Li, Z.-Q. Guo, X.-X. Zhang, and W.-B. Chang,** (2002). *A new competitive enzyme-linked immunosorbent assay (ELISA) for determination of estrogenic bisphenols.* Talanta, 57(6): p. 1205-1210.

[131] **Maiolini, E., E. Ferri, A.L. Pitasi, A. Montoya, M. Di Giovanni, E. Errani, and S. Girotti,** (2014). *Bisphenol A determination in baby bottles by chemiluminescence enzyme-linked immunosorbent assay, lateral flow immunoassay and liquid chromatography tandem mass spectrometry.* Analyst, 139(1): p. 318-324.

[132] **Yang, K., Z. Liu, M. Mao, X. Zhang, C. Zhao, and N. Nishi,** (2005). *Molecularly imprinted polyethersulfone microspheres for the binding and recognition of bisphenol A.* Analytica chimica acta, 546(1): p. 30-36.

[133] **Jo, M., J.-Y. Ahn, J. Lee, S. Lee, S.W. Hong, J.-W. Yoo, J. Kang, P. Dua, D.-k. Lee, and S. Hong,** (2011). *Development of single-stranded DNA aptamers for specific bisphenol A detection.* Oligonucleotides, 21(2): p. 85-91.

[134] **Fan, H., Y. Li, D. Wu, H. Ma, K. Mao, D. Fan, B. Du, H. Li, and Q. Wei,** (2012). *Electrochemical bisphenol A sensor based on N-doped graphene sheets.* Analytica chimica acta, 711: p. 24-28.

[135] **Yin, H.-s., Y.-l. Zhou, and S.-y. Ai,** (2009). *Preparation and characteristic of cobalt phthalocyanine modified carbon paste electrode for bisphenol A detection.* Journal of Electroanalytical Chemistry, 626(1): p. 80-88.

[136] **Zheng, Z., Y. Du, Z. Wang, Q. Feng, and C. Wang,** (2013). *Pt/graphene–CNTs nanocomposite based electrochemical sensors for the determination of endocrine disruptor bisphenol A in thermal printing papers.* Analyst, 138(2): p. 693-701.

[137] **Tu, X., L. Yan, X. Luo, S. Luo, and Q. Xie,** (2009). *Electroanalysis of Bisphenol A at a Multiwalled Carbon Nanotubes-gold Nanoparticles Modified Glassy Carbon Electrode.* Electroanalysis, 21(22): p. 2491-2494.

[138] **Gao, Y., Y. Cao, D. Yang, X. Luo, Y. Tang, and H. Li,** (2012). *Sensitivity and selectivity determination of bisphenol A using SWCNT–CD conjugate modified glassy carbon electrode.* Journal of Hazardous Materials, 199: p. 111-118.

[139] **Rather, J.A. and K. De Wael,** (2013). *Fullerene-C 60 sensor for ultra-high sensitive detection of bisphenol-A and its treatment by green technology.* Sensors and Actuators B: Chemical, 176: p. 110-117.

[140] **Kuila, T., S. Bose, P. Khanra, A.K. Mishra, N.H. Kim, and J.H. Lee,** (2011). *Recent advances in graphene-based biosensors.* Biosensors and Bioelectronics, 26(12): p. 4637-4648.

[141] **Liu, Y., X. Dong, and P. Chen,** (2012). *Biological and chemical sensors based on graphene materials.* Chemical Society Reviews, 41(6): p. 2283-2307.

[142] **Ntsendwana, B., B. Mamba, S. Sampath, and O. Arotiba,** (2012). *Electrochemical detection of bisphenol A using graphene-modified glassy carbon electrode.* International Journal of Electrochemical Science, 7(4): p. 3501-3512.

[143] **Ndlovu, T., O.A. Arotiba, S. Sampath, R.W. Krause, and B.B. Mamba,** (2012). *An exfoliated graphite-based bisphenol A electrochemical sensor.* Sensors, 12(9): p. 11601-11611.

[144] **Niu, X., W. Yang, G. Wang, J. Ren, H. Guo, and J. Gao,** (2013). *A novel electrochemical sensor of bisphenol A based on stacked graphene nanofibers/gold nanoparticles composite modified glassy carbon electrode.* Electrochimica Acta, 98: p. 167-175.

[145] **Gill, R., M. Zayats, and I. Willner,** (2008). *Semiconductor quantum dots for bioanalysis.* Angewandte Chemie International Edition, 47(40): p. 7602-7625.

[146] **Yin, H., Y. Zhou, S. Ai, Q. Chen, X. Zhu, X. Liu, and L. Zhu,** (2010). *Sensitivity and selectivity determination of BPA in real water samples using PAMAM dendrimer and CoTe quantum dots modified glassy carbon electrode.* Journal of Hazardous Materials, 174(1): p. 236-243.

[147] **Nambiar, S. and J.T. Yeow,** (2011). *Conductive polymer-based sensors for biomedical applications.* Biosensors and Bioelectronics, 26(5): p. 1825-1832.

[148] **Browne, D.J., L. Zhou, J.H. Luong, and J.D. Glennon,** (2013). *CE with a boron-doped diamond electrode for trace detection of endocrine disruptors in water samples.* Electrophoresis, 34(14): p. 2025-2032.

[149] **Zhang, Y., Y. Cheng, Y. Zhou, B. Li, W. Gu, X. Shi, and Y. Xian,** (2013). *Electrochemical sensor for bisphenol A based on magnetic nanoparticles decorated reduced graphene oxide.* Talanta, 107: p. 211-218.

[150] **Justino, C.I., T.A. Rocha-Santos, S. Cardoso, and A.C. Duarte,** (2013). *Strategies for enhancing the analytical performance of nanomaterial-based sensors.* TrAC Trends in Analytical Chemistry, 47: p. 27-36.

[151] **Yu, C., L. Gou, X. Zhou, N. Bao, and H. Gu,** (2011). *Chitosan–Fe 3 O 4 nanocomposite based electrochemical sensors for the determination of bisphenol A.* Electrochimica Acta, 56(25): p. 9056-9063.

[152] **Ma, Y., J. Liu, and H. Li,** (2017). *Diamond-based electrochemical aptasensor realizing a femtomolar detection limit of bisphenol A.* Biosensors and Bioelectronics, 92: p. 21-25.

[153] **Wang, F., J. Yang, and K. Wu,** (2009). *Mesoporous silica-based electrochemical sensor for sensitive determination of environmental hormone bisphenol A.* Analytica Chimica Acta, 638(1): p. 23-28.

[154] **Wang, W., X. Yang, Y.-x. Gu, C.-f. Ding, and J. Wan,** (2015). *Preparation and properties of bisphenol A sensor based on multiwalled carbon nanotubes/Li4Ti5O12-modified electrode.* Ionics, 21(3): p. 885-893.

[155] **Sumriddetchkajorn, S. and Y. Intaravanne,** (2012). *Home-made n-channel fiber-optic spectrometer from a web camera.* Applied spectroscopy, 66(10): p. 1156-1162.

[156] **McGonigle, A.J., T.C. Wilkes, T.D. Pering, J.R. Willmott, J.M. Cook, F.M. Mims, and A.V. Parisi,** (2018). *Smartphone Spectrometers.* Sensors, 18(1): p. 223.

[157] **Talukder, N., A. Furniturewalla, T. Le, M. Chan, S. Hirday, X. Cao, P. Xie, Z. Lin, A. Gholizadeh, and S. Orbine,** (2017). *A portable battery powered microfluidic impedance cytometer with smartphone readout: towards personal health monitoring.* Biomedical microdevices, 19(2): p. 36.

[158] **Sumriddetchkajorn, S., K. Chaitavon, and Y. Intaravanne,** (2014). *Mobile-platform based colorimeter for monitoring chlorine concentration in water.* Sensors and Actuators B: Chemical, 191: p. 561-566.

[159] **Sumriddetchkajorn, S., K. Chaitavon, and Y. Intaravanne,** (2013). *Mobile device-based self-referencing colorimeter for monitoring chlorine concentration in water.* Sensors and Actuators B: Chemical, 182: p. 592-597.

[160] **Intaravanne, Y. and S. Sumriddetchkajorn,** (2015). *Android-based rice leaf color analyzer for estimating the needed amount of nitrogen fertilizer.* Computers and Electronics in Agriculture, 116: p. 228-233.

[161] **Solmaz, M.E., A.Y. Mutlu, G. Alankus, V. Kılıç, A. Bayram, and N. Horzum,** (2018). *Quantifying colorimetric tests using a smartphone app based on machine learning classifiers.* Sensors and Actuators B: Chemical, 255: p. 1967-1973.

[162] **Jung, Y., J. Kim, O. Awofeso, H. Kim, F. Regnier, and E. Bae,** (2015). *Smartphone-based colorimetric analysis for detection of saliva alcohol concentration.* Applied optics, 54(31): p. 9183-9189.

[163] **Oncescu, V., D. O'Dell, and D. Erickson,** (2013). *Smartphone based health accessory for colorimetric detection of biomarkers in sweat and saliva.* Lab on a Chip, 13(16): p. 3232-3238.

[164] **Smith, G.T., N. Dwork, S.A. Khan, M. Millet, K. Magar, M. Javanmard, and A.K.E. Bowden,** (2016). *Robust dipstick urinalysis using a low-cost, micro-volume slipping manifold and mobile phone platform.* Lab on a Chip, 16(11): p. 2069-2078.

[165] **Mutlu, A.Y., V. Kılıç, G.K. Özdemir, A. Bayram, N. Horzum, and M.E. Solmaz,** (2017). *Smartphone-based colorimetric detection via machine learning.* Analyst, 142(13): p. 2434-2441.

[166] **Ozdemir, G.K., A. Bayram, V. Klc, N. Horzum, and M.E. Solmaz,** (2017). *Smartphone-based detection of dyes in water for environmental sustainability.* Analytical Methods, 9(4): p. 579-585.

[167] **McCracken, K.E., T. Tat, V. Paz, and J.-Y. Yoon,** (2017). *Smartphone-based fluorescence detection of bisphenol A from water samples.* RSC Advances, 7(15): p. 9237-9243.

[168] **Sawyer, C., P. McCarty, and G. Parkin,** (2003), *Chemistry for Environmental Engineering and Science.* McGraw-Hill Education.

[169] **USGS,** (2017), *Turbidity.* The United States Geological Survey: The USGS Water Science School.

[170] **WHO,** (2017), *Turbidity Measurement,* in *World Health Organization Fact Sheet 2.33.* World Health Organization.

[171] (1993), *Method 180.1: Determination of Turbidity by Nephelometry,* O.O.R.A. Development, Editor. United States Environmental Protection Agency: Cincinnati, Ohio.

[172] **O'Dell, J.W.,** (1993). *Method 180.1: Determination of turbidity by nephelometry.* Environmental Monitoring Systems Laboratory Office of Research and Development, US Environmental Protection Agency, Cincinnati, OH, 8.

[173] **Hussain, I., K.U. Ahamad, and P. Nath,** (2017). *Low-Cost, Robust, and Field Portable Smartphone Platform Photometric Sensor for Fluoride Level Detection in Drinking Water.* Analytical Chemistry, 89(1): p. 767-775.

[174] **Levin, S., S. Krishnan, S. Rajkumar, N. Halery, and P. Balkunde,** (2016). *Monitoring of fluoride in water samples using a smartphone.* Science of The Total Environment, 551–552: p. 101-107.

[175] **Hussain, I., M. Das, K.U. Ahamad, and P. Nath,** (2017). *Water salinity detection using a smartphone.* Sensors and Actuators B: Chemical, 239: p. 1042-1050.

[176] **Dutta, S., D. Sarma, and P. Nath,** (2015). *Ground and river water quality monitoring using a smartphone-based pH sensor.* AIP Advances, 5(5): p. 057151.

[177] **Hossain, M.A., J. Canning, S. Ast, P.J. Rutledge, and A. Jamalipour,** (2015). *Early warning smartphone diagnostics for water security and analysis using real-time pH mapping.* Photonic Sensors, 5(4): p. 289-297.

[178] **Koydemir, H.C., Z. Gorocs, D. Tseng, B. Cortazar, S. Feng, R.Y.L. Chan, J. Burbano, E. McLeod, and A. Ozcan,** (2015). *Rapid imaging, detection and quantification of Giardia lamblia cysts using mobile-phone based fluorescent microscopy and machine learning.* Lab on a chip, 15(5): p. 1284-1293.

[179] **San Park, T. and J.-Y. Yoon,** (2015). *Smartphone detection of Escherichia coli from field water samples on paper microfluidics.* IEEE Sensors Journal, 15(3): p. 1902-1907.

[180] **Gunda, N.S.K., S. Naicker, S. Shinde, S. Kimbahune, S. Shrivastava, and S. Mitra,** (2014). *Mobile Water Kit (MWK): a smartphone compatible low-cost water monitoring system for rapid detection of total coliform and E. coli.* Analytical Methods, 6(16): p. 6236-6246.

[181] **Hussain, I., K.U. Ahamad, and P. Nath,** (2016). *Water turbidity sensing using a smartphone.* RSC Advances, 6(27): p. 22374-22382.

[182] Grasse, E.K., M.H. Torcasio, and A.W. Smith, (2015). *Teaching UV–vis spectroscopy with a 3D-printable Smartphone spectrophotometer.* Journal of Chemical Education, 93(1): p. 146-151.

CURRICULUM VITAE

Abdullah Bayram

Balatçık Mahallesi Havaalanı Şosesi No: 33/2 Balatçık 35620 Çiğli İZMİR

Email: abdullahbayram7@gmail.com, abdullah.bayram@ikc.edu.tr

List of Publications:

1. Özdemir, Gizem Kocakuşak, **Abdullah Bayram**, Volkan Kılıç, Nesrin Horzum, and Mehmet E. Solmaz. "Smartphone-based detection of dyes in water for environmental sustainability." Analytical Methods 9, no. 4 (2017): 579-585

2. **Abdullah Bayram**, Cebrail Özbek, Mehmet Şenel, and Salih Okur. "CO gas sorption properties of ferrocene branched chitosan derivatives." Sensors and Actuators B: Chemical 241 (2017): 308-313.

3. Ali Y. Mutlu, Volkan Kılıç, Gizem Kocakuşak Özdemir, **Abdullah Bayram**, Nesrin Horzum, and Mehmet E. Solmaz. "Smartphone-based colorimetric detection via machine learning." Analyst 142, no. 13 (2017): 2434-2441

4. Solmaz, Mehmet E., Ali Y. Mutlu, Gazihan Alankus, Volkan Kılıç, **Abdullah Bayram**, and Nesrin Horzum. "Quantifying colorimetric tests using a smartphone app based on machine learning classifiers." Sensors and Actuators B: Chemical 255 (2018): 1967-1973.

5. **Abdullah Bayram,** Murat Serhatlioglu, Bulend Ortac, Serafettin Demic, Caglar Elbuken, Mustafa Sen, and Mehmet Ertugrul Solmaz. "Integration of glass micropipettes with a 3D printed aligner for microfluidic flow cytometer." Sensors and Actuators A: Physical 269 (2018): 382-387.

6. **Abdullah Bayram,** Nesrin Horzum, Aysegul Ulku Metin, Volkan Kılıç, and Mehmet Ertugrul Solmaz. "Colorimetric Bisphenol-A Detection with a Portable Smartphone-Based Spectrometer." IEEE Sensors Journal (2018).

7. **Abdullah Bayram,** Eyup Yalcin, Serafettin Demic, Orhan Gunduz, and Mehmet E. Solmaz, "Development and application of a low-cost smartphone-based turbidimeter using scattered light," Appl. Opt. 57, 5935-5940 (2018).

8. Volkan Kılıç, Gazihan Alankus, Nesrin Horzum, Ali Y. Mutlu, **Abdullah Bayram**, and Mehmet E. Solmaz. "Single-Image-Referenced Colorimetric Water Quality Detection Using a Smartphone." ACS Omega 3, no. 5 (2018): 5531-5536.